THE JOURNAL OF PHYSICAL CHEMISTRY C

Article

Cite This: J. Phys. Chem. C 2020, 124, 1717−1731

pubs.acs.org/JPCC

Förster Resonance Energy Transfer between Colloidal $CuInS_2$/ZnS Quantum Dots and Dark Quenchers

Chenghui Xia,[†,∥,⊥] Wentao Wang,[‡,§] Liang Du,[‡] Freddy T. Rabouw,[†] Dave J. van den Heuvel,[†] Hans C. Gerritsen,[†] Hedi Mattoussi,[‡] and Celso de Mello Donega*[,†]

[†]Debye Institute for Nanomaterials Science, Utrecht University, P.O. Box 80000, 3508 TA, Utrecht, The Netherlands

[‡]Department of Chemistry and Biochemistry, Florida State University, Tallahassee, Florida 32306, United States

Supporting Information

ABSTRACT: Förster resonance energy transfer (FRET) using colloidal semiconductor quantum dots (QDs) and dyes is of importance in a wide range of biological and biophysical studies. Here, we report a study on FRET between $CuInS_2$/ZnS QDs and dark quencher dye molecules (IRDye QC-1). Oleate-capped QDs with photoluminescence quantum yields (PLQYs) of 55 ± 4% are transferred into water by using two types of multifunctional polymer ligands combining imidazole groups and specific moieties with amine or methoxy groups as the terminal sites. The resulting water-dispersible QDs show PLQYs as high as 44 ± 4% and exhibit long-term colloidal stability (at least 10 months at 4 °C in the dark) with a hydrodynamic diameter of less than 20 nm. A side-by-side comparison experiment was performed using the amine or methoxy-functionalized QDs for coupling to dark quencher dye molecules. The amine-functionalized QDs bind to the dye molecules via covalent bonds, while methoxy-functionalized ones bind only weakly and nonspecifically. The progressive quenching of the QD emission and shortening of its photoluminescence decay time upon increasing the number of conjugated dye molecules demonstrate that the QD acts as the energy donor and the dark quencher dye as the energy acceptor in a donor−acceptor FRET pair. The FRET dynamics of the QD−dye conjugates are simulated using two different models based on the possible origin of the multiexponential PL decay of the QDs (i.e., variations in nonradiative or radiative decay rates). The model based on the radiative decay rates provides a better fit of our experimental data and estimates a donor−acceptor distance (6.5 nm) that matches well the hydrodynamic radius of the amine-functionalized QDs.

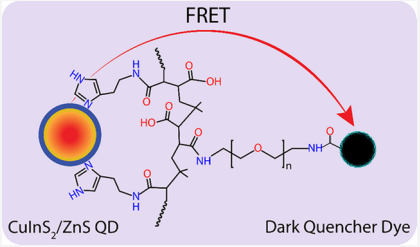

INTRODUCTION

Colloidal semiconductor quantum dot (QD)-based Förster resonance energy transfer (FRET) has been studied for a wide range of applications, such as biomedical imaging,[1−4] photodynamic therapy,[4−7] light harvesting,[4,8,9] and diagnostic and sensing devices.[4,10−12] The QD in a FRET pair can act as either an energy donor or an energy acceptor upon coupling to, for example, lanthanide complexes and lanthanide-doped nanoparticles,[13−17] fluorescent dye molecules,[2,8−10,18−25] or bioluminescent enzymes.[26,27] Among those, a QD donor paired with an organic dye acceptor is attractive since QDs can be excited over a wide spectral range with high absorption cross sections, making it possible to excite them at wavelengths where absorption by the dye molecule is minimal, thus minimizing the direct excitation of the acceptor and enhancing FRET sensitivity.[3,4,13,28] Moreover, the tunable photoluminescence (PL) of QDs provides flexibility in optimizing spectral overlap between the emission of QD donors and absorption of dye acceptors, thereby avoiding crosstalk between the FRET donor and acceptor.[3,4,13,28]

To date, the most commonly used QDs for FRET-based probes and sensors are CdX-based (X = Se, Te),[1,4] which are however of restricted applicability due to the high toxicity of Cd ions.[1,4] Nontoxic alternatives are thus highly needed but are still underdeveloped. Recently, copper indium sulfide ($CuInS_2$) QDs have attracted much attention since they combine low toxicity,[29−31] high PL quantum yields (PLQYs, ∼80% at 590 nm,[32] ∼75% at 810 nm,[33] ∼25% at 1050 nm[33]), large absorption coefficients (∼10^5 M^{-1} cm^{-1} at the first excitonic transitions),[34] and unparalleled PL tunability from visible to the near-infrared biological window (500−1100 nm).[35] These advantages make $CuInS_2$ QDs a promising alternative to CdX-based QDs for biomedical imaging applications.

Nonetheless, achieving robust colloidal stability for hydrophilic QDs under ambient conditions while keeping a compact hydrodynamic size is challenging, which has motivated extensive research over the past decade.[1,4] Post-synthetic ligand exchange is commonly used to transfer ZnS-capped QDs into water using ligands with thiol (-SH) head groups due to their strong affinity for Zn-rich surfaces.[33,36−40] Monothiol ligands, however, tend to oxidize and desorb from the surface of the QDs with time, potentially leading to particle aggregation and PL quenching.[36−38,41] Encapsulation of the

Received: November 10, 2019
Revised: December 17, 2019
Published: December 18, 2019

DOI: 10.1021/acs.jpcc.9b10536
J. Phys. Chem. C 2020, 124, 1717−1731

QDs within amphiphilic polymers or phospholipid micelles has also been reported to make them dispersible in water.[2,36,42] The hydrodynamic sizes of the product QDs are however quite large, resulting in low FRET rates, since these are strongly dependent on the donor−acceptor distance.[4] Recently, polymer ligands containing multiple imidazole (or pyridine) groups have been developed that provide an attractive alternative to thiol ligands and amphiphilic polymers as hydrophilic ligands to obtain water-dispersible CdSe/ZnS QDs.[23,24] As the imidazole groups are more resistant to oxidation than thiol groups, the resultant hydrophilic QDs show improved long-term (at least 1 year) colloidal stability at very low concentrations (10 nM) under ambient conditions (room temperature and ambient light).[23,24] They also exhibit good biocompatibility and compact hydrodynamic size (∼10 to 20 nm diameter for green-emitting QDs).[23,24] Owing to these advantageous characteristics, this new class of ligands was chosen in the present study to obtain water-dispersible $CuInS_2$/ZnS core/shell QDs by post-synthetic ligand exchange.

Previous works on CdX-based QDs have demonstrated that the assembly of multiple acceptor dyes at the surface of a QD increases the overall FRET efficiency.[18,43−46] However, this may also result in energy transfer between neighboring dye molecules,[44] leading to self-quenching of the dye emission, which complicates the analysis and extraction of the FRET rates. The use of non-fluorescent dyes as energy acceptors provides an effective way to prevent complications due to crosstalk between acceptors. In our work, we chose a commercial quencher dye molecule, IRDye QC-1,[47] as the energy acceptor. This dye absorbs light over a broad spectral range (600−1000 nm), which overlaps with the emission of $CuInS_2$ QDs while not emitting any light. This characteristic is of interest not only because it eliminates crosstalk between acceptors but also because it allows circumventing the inherent limitations of $CuInS_2$ QDs as donors: $CuInS_2$ QDs exhibit broad PL bandwidths (∼200 to 300 meV) and a low-energy tail in the absorption spectrum,[35] which may lead to crosstalk between donor and acceptor due to simultaneous detection of QD and dye emission, and bleed-through in excitation caused by reabsorption of dye emission by QDs. As the IRDye QC-1 dark quencher dye only absorbs light without any emission, crosstalk between acceptors and between donors and acceptors as well as excitation bleed-through is no longer relevant, which greatly simplifies the extraction of the FRET rates.

In this report, we describe a novel strategy for assembling FRET pairs using $CuInS_2$/ZnS QDs and dark quencher IRDye QC-1 dye molecules. The $CuInS_2$/ZnS core/shell QDs are synthesized by a sequential multistage method and have PLQYs of 55 ± 4%. These QDs are transferred into water through the exchange of the native oleate ligands for multifunctional polymer ligands combining imidazole groups and specific moieties with amine or methoxy groups as the terminal sites. The ligand exchange yields robust, compact, and bright QDs (e.g., PLQYs of 44 ± 4% for amine-terminated QDs) that are suitable for coupling to dark quencher dye molecules via covalent coupling between the amine groups and *N*-hydroxysuccinimide ester (NHS) groups. We found that the FRET efficiency increases with the number of dyes attached per QD. This study thus sheds light on designing novel Cd-free QD-based FRET nanoprobes, which is beneficial to a wide range of biological and biophysical studies.[1−12] Overall, the PL quenching data for these ternary QDs was successfully interpreted within the Förster dipole−dipole coupling model, as has been done before for CdSe-based QDs.[18−25] This is very relevant because it shows that the point-dipole approximation of the exciton is also valid in quantum dots of I-III-VI_2 semiconductors despite the disparate nature of the exciton radiative recombination in these materials with respect to QDs of II-VI semiconductors.[35,48] It is important to note that the nature of the radiative recombination in $CuInS_2$ (and other I-III-VI_2) nanocrystals has been under intense debate in the literature.[48] The observations reported in the present work provide an important contribution to this debate since they are consistent with a model recently proposed for the emission in $CuInS_2$ nanocrystals, which involves the radiative recombination of a delocalized conduction band electron with a hole localized at a Cu cation.[48]

EXPERIMENTAL SECTION

Materials. Copper (I) iodide (CuI, 98%), indium acetate ($In(Ac)_3$, 99.99%), zinc acetate dihydrate ($Zn(Ac)_2{\cdot}H_2O$, 98%), zinc iodide (ZnI_2), sulfur powder (99.98%), 1-dodecanethiol (DDT, 98%), 1-octadecene (ODE, 90%), trioctylphosphine (TOP, 90%), oleic acid (OA, 90%), poly(isobutylene-*alt*-maleic anhydride) [PIMA, average MW, ∼6000, 12−200 mesh (85%)], histamine (97%), *N*,*N*-dimethylformamide (DMF, 99.8%), deuterated chloroform ($CDCl_3$, 99.8 atom % D), deuterium oxide (D_2O, 99.9 atom% D), dimethyl sulfoxide (DMSO, 99.9%), anhydrous toluene, methanol, and butanol were purchased from Sigma-Aldrich. Lumogen red 305 (article no. 94720) and the IRDye QC-1 dark quencher dye were purchased from Kremer Pigmente GmbH & Co. KG and LI-COR Biosciences, respectively. ODE and OA were degassed at 120 °C for 3 h prior to use. The precursors H_2N-PEG_{750}-OCH_3 and H_2N-PEG_{600}-NH_2 were synthesized starting from poly(ethylene glycol) methyl ether (average MW, ∼750 Da) and poly(ethylene glycol) (average MW ∼600 Da), respectively, following previously reported procedures.[49,50] Other reagents were used as received. The syntheses were performed in a standard Schlenk line.

Synthesis of His-PIMA-PEG/OMe (50% His and 50% NH_2-PEG-OMe). The polymer ligands were synthesized following the method reported by Wang and co-workers.[23,24] In brief, solution A was prepared by dissolving PIMA (0.385 g, ∼2.5 mmol monomer units) in 10 mL of anhydrous DMF. The solution was loaded into a three-neck flask and heated to 40 °C under N_2 flow. In the meantime, solution B was prepared by mixing histamine (0.139 g, 1.25 mmol) and NH_2-PEG-OMe (0.941 g, 1.25 mmol) in 2 mL of DMF. Solution B was dropwise added to solution A, and the mixture was stirred overnight at 40 °C. Then, the solvent was removed under vacuum, and the crude reaction product was dispersed in 3 mL of anhydrous chloroform. The resulting solution was loaded onto a silica column, and the compound was purified with chloroform as the eluent. Evaporating the solvent yielded a yellow gel-like product.

His-PIMA-PEG/NH_2 (50% His, 40% NH_2-PEG-OMe, and 10% NH_2-PEG-NH_2). The amine-functionalized polymer ligands were synthesized following a modification of the procedure mentioned above. Specifically, solution A was prepared by dissolving PIMA (0.385 g, ∼2.5 mmol monomer units) in 10 mL of anhydrous DMF. The solution was loaded into a three-neck flask and heated to 40 °C under N_2 flow. Meanwhile, solution B was prepared by dissolving histamine (0.139 g, 1.25 mmol) and H_2N-PEG-OMe (0.377 g, 0.5

DOI: 10.1021/acs.jpcc.9b10536
J. Phys. Chem. C 2020, 124, 1717−1731

mmol) in 2 mL of DMF, and solution C was obtained by dissolving H_2N-PEG-OMe (0.377 g, 0.5 mmol) and NH_2-PEG-NH_2 (0.150 g, 0.25 mmol) in 2 mL of DMF. To the flask containing solution A, the as-prepared solution B was dropwise added, and the mixture was kept stirring for 1 h at 40 °C. Subsequently, solution C was also dropwise added to this mixture. The reaction mixture was left stirring overnight at 40 °C, followed by purification using the same procedure described above.

Synthesis of $CuInS_2$ Core QDs. The $CuInS_2$ core QDs were synthesized following a previously reported method.[51] CuI (190 mg, 1 mmol), $In(Ac)_3$ (292 mg, 1 mmol), and DDT (10 mL) were degassed at 60 °C for 2 h. Then, the reaction flask was purged with N_2 and heated to 230 °C. The mixture was allowed to react for 25 min and then cooled down to 210 °C for further synthesis.

Synthesis of Alloy (Cu,In,Zn)S_2 QDs. Prior to synthesis, the ZnS stock solution was prepared by dissolving ZnI_2 (1629 mg, 5 mmol) and S/TOP (160 mg of S in 5 mL of TOP) into 5 mL of ODE. Gradient alloy (Cu,In,Zn)S_2 QDs were synthesized by slowly injecting the as-prepared ZnS precursors (0.5 mL/min) into the preformed $CuInS_2$ QD solution at 210 °C. The reaction mixture was kept at 210 °C for 2 h followed by naturally cooling down to room temperature. The crude products were washed twice by repeated precipitation with an isometric butanol and methanol mixture and redispersion into toluene. The purified products were dried under vacuum for 2 h.

Synthesis of $CuInS_2$/ZnS Core/Shell QDs. The gradient alloy (Cu,In,Zn)S_2 QDs were coated with additional ZnS shells through a SILAR method at 230 °C. The Zn solution (0.25 mmol/g) was prepared by degassing a mixture of $Zn(Ac)_2 \cdot H_2O$ (2.19 g, 10 mmol) into OA (6.21 g, 22 mmol) and ODE (33 g) at 140 °C for 2 h. The S solution (0.5 M) was prepared by dissolving S powder (0.321 g, 10 mmol) into ODE (20 mL) at 180 °C. For a typical $CuInS_2$/ZnS core/shell QD synthesis, all of the dried gradient alloy (Cu,In,Zn)S_2 QD products were redispersed in a mixed solution of DDT (2 mL) and ODE (8 mL) in a 100 mL three-neck flask. The reaction mixture was heated to 230 °C for the injections. The first injection cycle was 1 mL of Zn solution (~0.2 mmol) followed by injecting 400 μL of S solution (0.2 mmol) after 10 min. This injection procedure was repeated five times with an interval time of 10 min. After the injections, the reaction mixture was annealed at 230 °C for another hour. Finally, the crude reaction products were cooled down to room temperature and were washed three times by using the same washing procedure described above for alloy (Cu,In,Zn)S_2 QDs. The purified QDs were dried under vacuum to obtain ~1.2 g of red powder. The product $CuInS_2$/ZnS core/shell QDs were redispersed in 20 mL of anhydrous toluene, yielding a 60 mg/mL (4.74×10^{-4} M) stock solution. The QD concentration was estimated by absorption spectrophotometric analysis according to the previous literature.[34]

Ligand Exchange. The ligand exchange reaction was performed using an adaptation of the protocol reported by Wang et al.[23,24] Typically, 50 μL of the as-prepared stock solution of $CuInS_2$/ZnS QDs (3 mg of QDs) was dried and redispersed in 300 μL of chloroform. Then, 25 mg of His-PIMA-PEG/NH_2 or His-PIMA-PEG/OMe dissolved in 300 μL of chloroform was added to the QD solution. This homogeneous mixture was stirred (600 rpm) at room temperature overnight. After that, the QDs were precipitated by adding 400 μL of methanol and 4 mL of hexane followed by centrifugation at 3600 rpm for 7 min. The top layer of solvents was removed, and the red precipitate was redispersed in 300 μL of chloroform and 300 μL of methanol followed by addition of 4 mL of hexane. The resulting turbid solution was sonicated for 1 min and centrifuged at 3600 rpm for 7 min. The supernatant was discarded, and the precipitate was dried under vacuum for 10 min to obtain a red pellet. This pellet was redispersed in 4 mL of deionized water (18.2 MΩ·cm at 25 °C), and the clear QD solution was filtered through a disposable syringe filter (pore size 0.45 μm). The excess free ligands were removed by applying three rounds of concentration/dilution using a centrifugal filtration device (Millipore, MW cutoff = 50 kDa) by centrifugation at 3600 rpm for 9 min. Finally, the purified QDs were dispersed in 2 mL of deionized water and stored in the dark at 4 °C for further use. The QD concentration (~13 μM) was estimated according to the literature.[34] The ligand exchange approach can be scaled up 10 times by increasing the amount of each component while keeping all the ratios fixed. Briefly, 500 μL of the as-prepared stock solution of $CuInS_2$/ZnS QDs (30 mg of QDs) was dried and redispersed in 3 mL of chloroform. Then, 250 mg of His-PIMA-PEG/NH_2 or His-PIMA-PEG/OMe dissolved in 3 mL of chloroform was added to the QD solution. This homogeneous mixture was stirred (600 rpm) at room temperature overnight. The products were purified using the same procedure described above and finally dispersed in 4 mL of deionized water.

Conjugation of QDs to IRDye QC-1 Dark Quencher. The amino group of water-soluble QDs reacted with the NHS ester group of the IRDye QC-1 dark quencher dye to provide the QD−dye conjugate. The preformed amine-functionalized His-PIMA-PEG/NH_2-capped QDs (900 μL; ~13.05 μM) were transferred into 900 μL of potassium phosphate buffer (50 mM, pH = 8.5 at 25 °C) by applying two rounds of concentration/dilution using a centrifugal filtration device (Millipore, MW cutoff = 50 kDa) by centrifugation at 3600 rpm for 9 min. The QDs (80 μL) in phosphate buffer were mixed with a certain amount of dye molecules (0−7.79 μL, 2.23 mg/mL in anhydrous DMSO) according to the dye/QD feeding molar ratios from 0 to 20 and then incubated overnight in the dark at 4 °C. Subsequently, the QD−dye conjugates were separated from free dye molecules and NHS byproducts via size-exclusion chromatography using G-25 columns, resulting in ~80 μL of QD−dye conjugates. A side-by-side control experiment was performed under the same conditions but using His-PIMA-PEG/OMe-capped QDs instead. To avoid inner filter effects, the optical density of the QD−dye conjugates at the excitation wavelength (445 nm) was kept below 0.05 by diluting 50 μL of the QD−dye eluates in 2 mL of deionized water for optical measurements.

Optical Spectroscopy. Samples for optical measurements were prepared by dissolving the QDs into 3 mL of anhydrous toluene or deionized water in 1 cm path length sealed quartz cuvettes. Absorption spectra were measured using a PerkinElmer Lambda 950 UV−vis−NIR spectrometer. PL spectra were recorded on an Edinburgh Instruments FLS920 spectrofluorometer. The PL spectra were corrected for the instrumental response. PL decay measurements were carried out in the same spectrofluorometer using an Edinburgh Instruments picosecond pulsed diode laser (EPL 445) operating at 441.4 nm (80.2 ps pulse width, 0.02−20 MHz repetition rate) as an excitation source, and a fast Hamamatsu

DOI: 10.1021/acs.jpcc.9b10536
J. Phys. Chem. C 2020, 124, 1717−1731

(a)

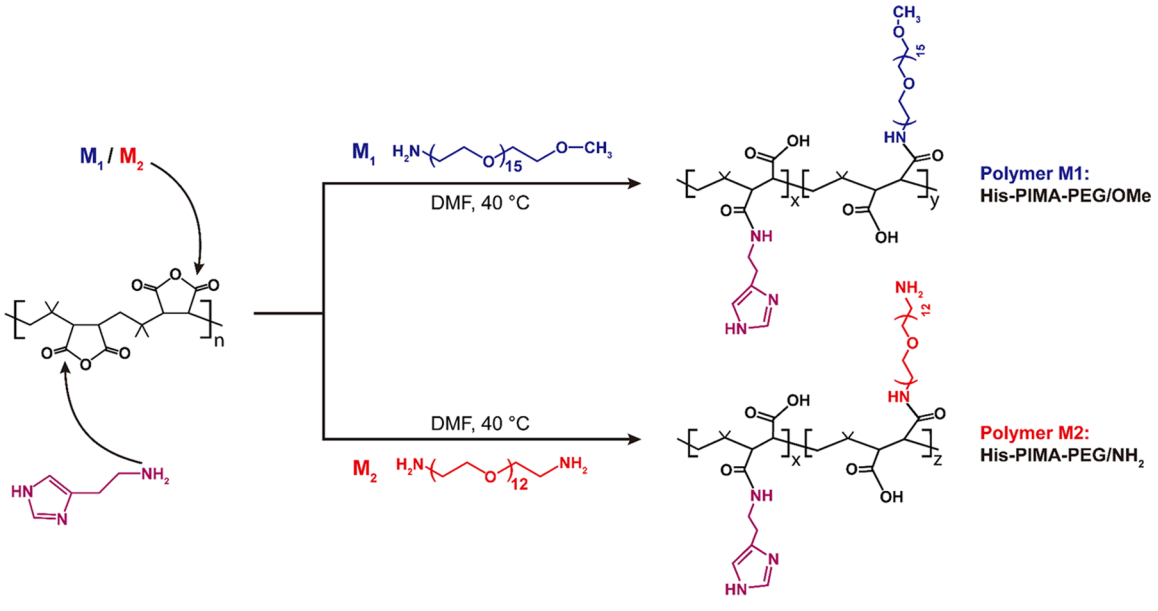

(b)

Polymer Name	Molar Fractions	Nominal Number per Chain	Experimental Number per Chain	Purity
His-PIMA-PEG/OMe	x:y = 50:50	His: 20 OMe: 20	His: 18 OMe: 19	~82%
His-PIMA-PEG/NH_2	x:y:z = 50:40:10	His: 20 OMe: 16 NH_2: 4	His: 19 OMe: 17 NH_2: ~(0−3)	~71%

Figure 1. (a) Schematic illustration of the nucleophilic addition reaction for preparing His-PIMA-PEG/OMe and His-PIMA-PEG/NH_2 polymer ligands. The His-PIMA-PEG/NH_2 was obtained by partially replacing NH_2-PEG-OMe for NH_2-PEG-NH_2. (b) Detailed information on the prepared ligands, including the feeding molar fractions of each functional groups (*x*: His; *y*: NH_2-PEG-OMe; *z*: NH_2-PEG-NH_2) with respect to the PIMA backbone, corresponding nominal and experimental numbers per PIMA chain, and the product purity. The experimental numbers per chain were estimated by comparing the ^{1}H NMR signal integrations of the three protons from the terminal methoxy group of the poly(ethylene glycol) (PEG) segments (3.37 ppm), the proton from imidazole rings (7.14 ppm), and the protons from methyl groups of PIMA chains (~1.04 ppm) (Supporting Information, Figure S1). The purity is the yield without purification, which was estimated using the information of grafting degree and the known amount of ferrocene in deuterated chloroform as a standard (Supporting Information, Figure S1).

photomultiplier tube (H7422−40) as the detector. A 455 nm long pass filter was fixed before the detector. The peak position of steady-state PL spectra of each sample was used as the detection wavelength for the PL decay measurements.

Photoluminescence Quantum Yields (PLQYs). The PLQYs were measured using Lumogen red 305 (PLQY = 95%) in anhydrous toluene as a standard. To avoid inner filter effects, the absorbances of QD and Lumogen red 305 solutions at and above the excitation wavelength (442 nm) were below 0.1. For each sample, five different concentrations were prepared. The PLQYs were calculated according to $\emptyset_X = \emptyset_{ST}\frac{Grad_X}{Grad_{ST}} \times \frac{R_X^2}{R_{ST}^2}$ where the subscripts ST and X denote standard and sample, respectively, $\emptyset$ is the PLQY, Grad is the gradient that was generated by linear fitting a scatter plot of integrated PL intensity versus the absorbance at excitation wavelength, and *n* is the refractive index of the solvent (toluene for Lumogen red 305 and toluene or water for the QDs).

Powder X-ray Diffraction (XRD). XRD results were obtained on Bruker D2 Phaser, equipped with a Co Kα X-ray source (1.79026 Å). Samples were washed at least 3 times, dried under vacuum overnight, and uniformly dispersed on a silicon wafer prior to the XRD measurements.

Nuclear Magnetic Resonance Spectroscopy (NMR). ^{1}H NMR measurements were performed using an Agilent MRF400 equipped with a OneNMR probe and an Optima Tune system. Spectra were collected using the following conditions: 400 MHz, 25 °C, a pulse repetition time of 25.0 s, a pulse width of 14.0 μs, and an acquisition time of 5 min. The hydrophobic samples were dried and dispersed in anhydrous $CDCl_3$, while hydrophilic samples were dissolved in D_2O. All samples have a volume of 500 μL. The concentration of organic molecules was 30 mg/mL. The QD concentration was ~40 μM. Ferrocene (0.2 M) was used as the reference for calculating the purity of product polymer ligands. Pyridine (0.1 M) was used as the reference for calculating the ligand density per QD.

Fourier Transform Infrared Spectroscopy (FTIR). FTIR spectra were measured from 400 to 4000 cm^{-1} (2 cm^{-1} resolution) for 400 scans using a vertex 70 FTIR spectrometer (BRUKER) equipped with a KBr/DLaTGS D301 detector. Approximately 0.1 to 1.0 wt % purified sample was well dispersed into 200−250 mg of fine KBr powder followed by grinding under an infrared lamp and pressing into a pellet.

Zeta Potential and Dynamic Light Scattering (DLS). Zeta potential and DLS measurements were conducted on a Malvern instrument Zetasizer Nano ZS using a DTS1070 folded capillary cell. The samples were loaded into the folded capillary cell after passing through Millex syringe filter units (pore size, 0.45 μm). To reduce the incident error, a sample was separately measured for three times with 20 scans for each measurement. The spectra were corrected by the instrument software for viscosity (0.8872 cP at 25 °C), absorption (at 532 nm), solvent (water), refractive index (1.33), and material

DOI: 10.1021/acs.jpcc.9b10536
J. Phys. Chem. C 2020, 124, 1717−1731

($CuInS_2$) refractive index (2.55). The hydrodynamic sizes were collected in automatic mode and expressed in number (%). The same settings were used to measure the zeta potential. The pH measurements were carried out on the line-powered 827 pH lab with Primatrode. The instrument was calibrated beforehand using standard pH calibration buffer solutions pH 4, 7, and 9. The pH value of a sample was obtained by averaging three measurements.

RESULTS AND DISCUSSION

Ligand Design. The polymer ligands were synthesized via a nucleophilic addition reaction by introducing histamine (His), amine-poly(ethylene glycol)-methoxy (NH_2-PEG-OMe, MW = 750 g/mol), and amine-poly(ethylene glycol)-amine (NH_2-PEG-NH_2, MW = 600 g/mol) to the maleic anhydride groups of the poly(isobutylene-*alt*-maleic anhydride) (PIMA) backbone (MW = 6000 g/mol; ~39 maleic anhydrides per chain), following previously reported procedures.[23,24] The nucleophilic addition reaction between amine groups and anhydride rings is highly efficient, allowing controlled insertion of specific moieties to the PIMA backbone. Moreover, the presence of dimethyl groups between adjacent *cis*–*trans* anhydride rings improves the reactivity and reduces the steric hindrance, leading to efficient addition reactions and compact configuration of polymer ligands.[23,24] The architecture of the product ligands is strongly dependent on the feeding ratios of the introduced segments with respect to PIMA. In this work, two types of polymer ligands (viz., His-PIMA-PEG/OMe and His-PIMA-PEG/NH_2) were prepared, as schematically depicted in Figure 1a. The polymer His-PIMA-PEG/OMe was obtained by reacting PIMA with a mixture of 50% His and 50% NH_2-PEG-OMe per chain. The polymer His-PIMA-PEG/NH_2 was synthesized by replacing 20% of the NH_2-PEG-OMe for NH_2-PEG-NH_2, viz., 50% His, 40% NH_2-PEG-OMe, and 10% NH_2-PEG-NH_2 per chain (the product is thus 80% His-PIMA-PEG/OMe and 20% His-PIMA-PEG/NH_2). The experimental numbers of the functional groups per chain were measured by ^{1}H nuclear magnetic resonance (NMR) spectroscopy [Figure 1b and Supporting Information, Figure S1]. The resulting values are consistent with the nominal values, demonstrating the high efficiency of the nucleophilic addition reactions. The purity of the His-PIMA-PEG/OMe and His-PIMA-PEG/NH_2 products is 82 and 71%, respectively (Figure 1b and Supporting Information, Figure S1). Different from the methoxy-terminated His-PIMA-PEG/OMe, the terminal $-NH_2$ groups of the product His-PIMA-PEG/NH_2 make the conjugation of the IRDye QC-1 dark quencher dye easier since it allows the use of NHS reaction chemistry. These two types of polymer ligands allow side-by-side comparison of the FRET process in chemically bound QD–dye conjugates (amine-terminated polymers) and in control systems in which the dye molecules and the QDs are only weakly interacting (methoxy-terminated polymers).

Colloidal Oleate Capped $CuInS_2$/ZnS QDs. The $CuInS_2$/ZnS QDs used in this study were synthesized by a multistage approach in three steps (Figure 2a). Briefly, preformed $CuInS_2$ QDs were used as cores for the overgrowth of a thin ZnS shell by using a mixture of zinc iodide and sulfur/trioctylphosphine in octadecene as ZnS precursors. This process yields gradient-alloy (Cu,In,Zn)S_2 QDs, which were further used as cores for additional ZnS shelling by a successive ion layer adsorption and reaction (SILAR) method at 230 °C (Figure 2a) (see the Experimental Section for details). Powder

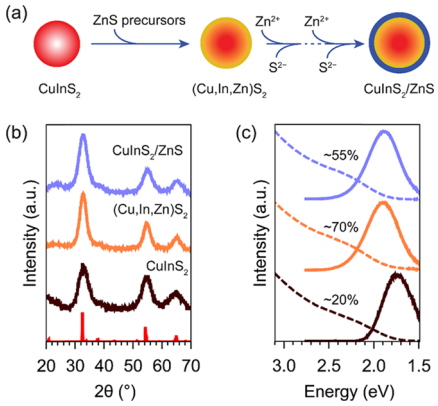

Figure 2. (a) Schematic diagram of the synthesis of $CuInS_2$/ZnS QDs. (b) XRD patterns of $CuInS_2$ QDs before and after ZnS shelling. The red line indicates standard PDF card (PDF Card–01–081–9515) of the chalcopyrite $CuInS_2$. (c) Absorption (dashed line) and PL (solid line) spectra of $CuInS_2$ QDs before and after ZnS shelling (color code is the same in panel (b)). The final product $CuInS_2$/ZnS QDs have PLQYs of 55 ± 4%.

X-ray diffraction (XRD, Figure 2b) and high-resolution transmission electron microscopy (HRTEM, Supporting Information, Figure S2a) demonstrate that the $CuInS_2$ QDs used as cores have the chalcopyrite crystal structure and a diameter of 3.2 nm, which agrees well with the size estimated from absorption spectrophotometric analysis (viz., 3.1 nm) using a previously reported sizing curve.[34] The chalcopyrite crystal structure is preserved after the first ZnS shelling cycle (Figure 2b), which is accompanied by an increase in diameter to 3.6 nm (Supporting Information, Figure S2), a shift of the absorption and PL spectra to higher energies (by 80 and 164 meV, respectively), and a pronounced improvement of the PLQY from 20 ± 2% (at 715 nm) to 70 ± 5% (at 642 nm) (Figure 2c and Supporting Information, Figure S3). Spectral blueshifts after ZnS shelling on $CuInS_2$ QDs have been previously reported in many studies and are ascribed to several reasons (e.g., partial Zn^{2+} for In^{3+} and Cu^+ cation exchange followed by interdiffusion,[32,33,52–55] shrinkage of the core due to either etching prior to the shell overgrowth[51,56] or shell ingrowth by cation exchange[52]). A detailed discussion of this topic can be found in previous papers.[33,55] Considering the nature of the ZnS precursors used for the first ZnS shelling cycle (i.e., a very reactive Zn precursor, ZnI_2, combined with a less reactive sulfur precursor, viz., sulfur/trioctylphosphine, in the presence of the Cu^+ extracting agent trioctylphosphine), we attribute the spectral blueshift observed in the present study to the formation of a gradient (Cu,In,Zn)S_2 alloy QD with a ZnS-rich surface since under these conditions, cation exchange followed by interdiffusion is expected to be the dominant process.[55] This is consistent with the small increase in diameter after the first shelling cycle (viz., 0.4 nm), which corresponds to a shell thickness of only 0.2 nm (equivalent to 0.6 monolayers of ZnS).

Following the first ZnS shelling cycle and after purification of the product (Cu,In,Zn)S_2 QDs, a SILAR method was adopted to further grow the ZnS shell using zinc oleate and sulfur/octadecene as the ZnS precursors (Figure 2a). The chalcopyrite crystal structure is preserved in the final $CuInS_2$/ZnS core/shell QDs (Figure 2b and Supporting Information, Figure S2c,d), showing that the ZnS overgrowth proceeds by heteroepitaxy (i.e., the ZnS shell adopts the zinc-blende

DOI: 10.1021/acs.jpcc.9b10536
J. Phys. Chem. C 2020, 124, 1717–1731

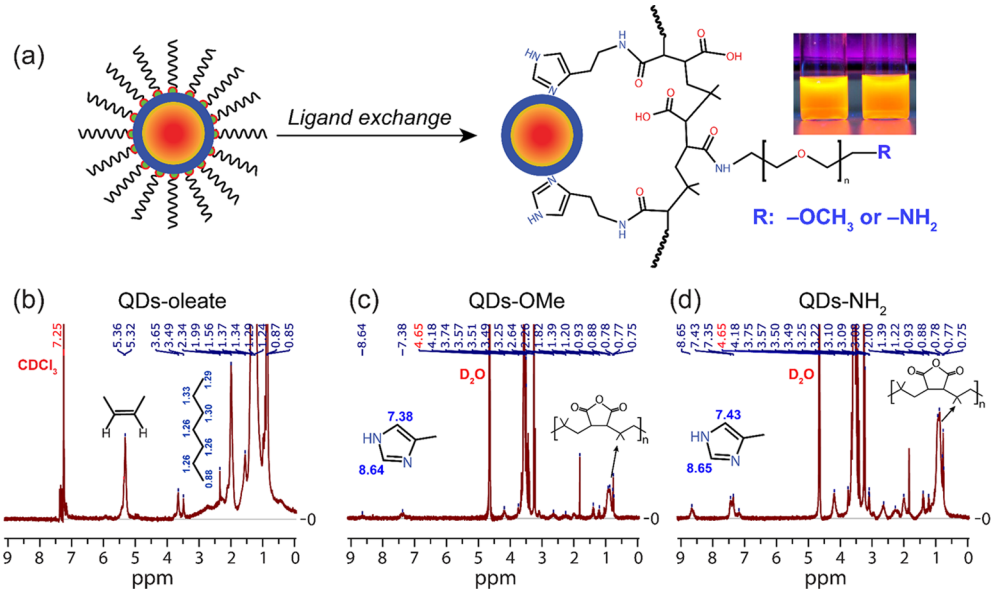

Figure 3. (a) Schematic diagram of the ligand exchange process. Hydrophobic $CuInS_2$/ZnS QDs were transferred to water upon exchange of native ligands for His-PIMA-PEG/OMe and His-PIMA-PEG/NH_2. Inset digital image is the water-dispersible QDs-OMe and QDs-NH_2 under a 405 nm ultraviolet lamp. (b) ^{1}H NMR spectrum of hydrophobic QDs-oleate. The broad peak at ∼5.3 ppm is ascribed to the protons from the C═C double bond. The strong signatures at ∼1.2 and 0.88 ppm are attributed to the resonances from the protons in the methylene groups and in the terminal methyl groups, respectively. Deuterated chloroform ($CDCl_3$) was used as the solvent. (c, d) ^{1}H NMR spectrum of QDs-OMe and QDs-NH_2, respectively. The weak broad resonances at ∼7.4 and ∼8.6 ppm are ascribed to the protons from the imidazole rings. The strong signatures at 3.57 and 3.25 ppm are attributed to the resonances from the protons in the PEG segments and in the terminal methoxy groups, respectively. Deuterium oxide (D_2O) was used as the solvent.

structure). The QD diameter increases from 3.6 to 4.2 nm (Supporting Information, Figure S2c,d), demonstrating that the gradient alloy (Cu,In,Zn)S_2 QDs are overcoated by 1 monolayer of ZnS during the SILAR cycle, bringing the total thickness of the ZnS shell to ∼1.6 ZnS monolayers. The PLQY of the product $CuInS_2$/ZnS core/shell QDs however decreases from 70 ± 5 to 55 ± 4% (peak at 645 nm), implying that new nonradiative recombination sites were generated during the SILAR cycle,[57,58] possibly due to diffusion of Cu and/or In atoms to the surface[54] since the small lattice mismatch between $CuInS_2$ and ZnS (2%) and the high diffusion rates in $CuInS_2$ facilitate interdiffusion.[55] These surface Cu or In atoms are likely less well passivated than in the original gradient alloy (Cu,In,Zn)S_2 cores because the second ZnS shelling cycle also results in replacement of the original capping ligands (dodecanethiol) by oleate, as evidenced by Fourier transform infrared spectroscopy, which clearly shows the asymmetric C(═O)O— stretching vibration of the carboxylic acid group from Zn(oleate)$_2$ at 1556 cm^{-1} (Supporting Information, Figure S4).

Exchange of the Native Ligands for the Designed Polymers. The oleate-capped $CuInS_2$/ZnS QDs (QDs-oleate) are transferred into water through exchange of the native ligands for His-PIMA-PEG/OMe and His-PIMA-PEG/NH_2.[23,24] This step results in two types of water-dispersible QDs: His-PIMA-PEG/OMe-capped QDs (QDs-OMe) and His-PIMA-PEG/NH_2-capped QDs (QDs-NH_2). Figure 3a shows the schematic diagram of the ligand exchange process. The imidazole rings serve as anchors onto the ZnS surface of the $CuInS_2$/ZnS QDs. As Zn^{2+} forms strong coordination bonds with the electron-donor groups of imidazole rings,[59,60] the ligand exchange can be readily completed at room temperature overnight. ^{1}H NMR spectra of $CuInS_2$/ZnS QDs before and after ligand exchange were acquired (Figure 3b–d). A pronounced broad C═C double bond resonance (∼5.3 ppm) coming from the surface oleate group disappears after transfer to water (Figure 3b–d). For the water-dispersible QDs, a broad peak is observed at ∼0.8 ppm, which is attributed to the protons from PIMA backbones (Figure 3c,d and Supporting Information, Figure S5). In addition, the characteristic peaks of imidazole rings (∼7.4 and ∼8.6 ppm) become broad compared with the ligand alone, demonstrating that the designed polymer ligands bind to the QDs through their imidazole groups (Figure 3c,d and Supporting Information, Figures S1 and S5). NMR spectroscopy was further employed to quantify the ligand coverage density on QDs by comparing the molar concentrations of the polymer ligands and the QDs. The QD molar concentration was calculated by absorption spectrophotometric analysis using molar absorption coefficients recently provided in the literature.[34] The original size of the $CuInS_2$ cores (3.1 nm) is not used for calculating the extinction coefficients of the $CuInS_2$/ZnS core/shell QDs because the sizes of the $CuInS_2$ cores are affected during the ZnS shelling, as evidenced by the spectral blueshift observed after the shelling reaction. As discussed above, this spectral blueshift reflects a reduction in the effective core diameter due to the formation of a gradient (Cu,In,Zn)S_2 alloy. Therefore, the effective diameter of the $CuInS_2$ cores (2.3 nm) is deduced from the first absorption transition energies combined with the sizing curve of chalcopyrite $CuInS_2$ QDs reported in the previous literature.[34] This effective core size is then used to obtain the QD molar concentration.[34] The molar concentration of polymer ligands was obtained by comparing the integrations of the methyl proton of the PIMA backbone and the γ-proton of the pyridine standard. This analysis yields a value of ∼10 His-PIMA-PEG/NH_2 ligands per QD, which corresponds to ∼195 imidazole anchors and ∼39 amines per QD (Supporting Information,

DOI: 10.1021/acs.jpcc.9b10536
J. Phys. Chem. C 2020, 124, 1717–1731

Figure S5). The same calculation was applied to the QDs-OMe, yielding ~3 His-PIMA-PEG/OMe per QD, which corresponds to ~59 imidazole anchors per QD (Supporting Information, Figure S5). The number of polymer ligands estimated for the His-PIMA-PEG-NH_2 is close to what was measured in previous studies.[23] We attribute the difference between the number of ligands per QD for the two types of ligands to batch-to-batch variations since the major ligands are His-PIMA-PEG-OMe in both cases as NH_2-modified ligands are prepared by reacting the PIMA precursor with a mixture of PEG-NH_2 and PEG-OMe.

After transfer to water, the absorption spectra of the hydrophilic $CuInS_2$/ZnS QDs remain nearly the same (Figure 4a), indicating that no aggregates are formed. The PL spectra

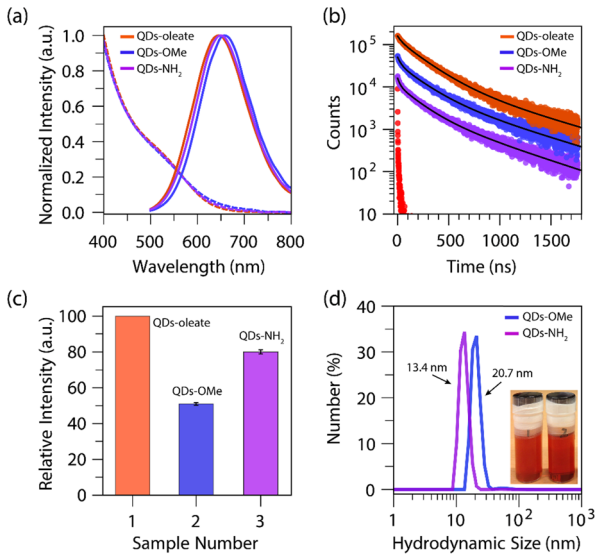

Figure 4. (a) Absorption (dashed line) and PL (solid line) spectra of $CuInS_2$/ZnS QDs before and after transfer to deionized water upon exchange of the native ligands for His-PIMA-PEG/OMe and His-PIMA-PEG/NH_2 polymer ligands. (b) PL decay curves of $CuInS_2$/ZnS QDs before and after ligand exchange. The instrument response function (IRF) is also shown (red dots). The decay curves are fitted by triple exponential functions. For QDs-oleate: τ_1 = 20 ns (2.6%), τ_2 = 140 ns (31.45%), τ_3 = 408 ns (65.95%), χ^2 = 1.027, average $\tau_{QDs\text{-}oleate}$ = 314 ns; for QDs-OMe: τ_1 = 17 ns (4.09%), τ_2 = 128 ns (35.65%), τ_3 = 400 ns (60.26%), χ^2 = 1.04, average $\tau_{QDs\text{-}OMe}$ = 287 ns; for QDs-NH_2: τ_1 = 15 ns (3.32%), τ_2 = 122 ns (29.84%), τ_3 = 394 ns (66.84%), χ^2 = 1.06, average $\tau_{QDs\text{-}NH2}$ = 300 ns. (c) Histogram plot of relative integrated PL intensity of QDs-oleate (PLQY of 55 ± 4%, peak at 645 nm), QDs-OMe (PLQY of 27 ± 3%, peak at 660 nm), and QDs-NH_2 (PLQY of 44 ± 4%, peak at 650 nm). The QD concentrations were kept the same. (d) Hydrodynamic diameters of QDs-OMe and QDs-NH_2. Inset is the product hydrophilic QDs obtained by scaled-up ligand exchange (see the Experimental Section for details).

are also essentially the same, apart from a small redshift (35 meV for QDs-OMe and 12 meV for QDs-NH_2) accompanied by a reduction in the PL intensity (Figure 4a,c). Redshifts in PL spectra are commonly observed after ligand exchange[61,62] and may be attributed to partial extension of the exciton wave function in the ligand shell, thereby relaxing its confinement within the QD. Reductions in PLQY upon transfer of QDs to water have also been widely reported and are commonly ascribed to the insufficient shell quality in part of the QD ensemble.[33,39] Nonetheless, the PLQYs of the polymer-capped $CuInS_2$/ZnS QDs (27 ± 3%, peak at 660 nm and 44 ± 4%, peak at 650 nm for QDs-OMe and QDs-NH_2, respectively) are comparable to those of other water-dispersible $CuInS_2$-based QDs and dyes previously reported in the literature.[30,31,33,62,63] Figure 4b shows that the PL decay is multiexponential, with decay times varying from ~20 ns to several hundreds of ns. The average exciton lifetime of $CuInS_2$/ZnS QDs decreases after the ligand exchange, reflecting an increase in the nonradiative recombination rates, which is consistent with the decrease of PLQYs (Figure 4b,c). It should be noted that, despite their multiexponential character, the PL decay curves of the $CuInS_2$/ZnS QDs studied in our work are very reproducible. The errors in the exciton lifetimes reported in Figure 4 (and throughout this work) thus originate primarily from the standard deviations in the fitting procedure, which are very small (≤5%). The resulting negatively charged QDs-NH_2 [ζ-potential, −(50 ± 5) mV] have a compact hydrodynamic diameter of ~13 nm, which increases to ~19 nm after storing in dark at 4 °C for 10 months (Figure 4d and SI, Figure S6). Moreover, TEM image shows that these QDs are well-dispersed and have an average size of 4.4 ± 0.7 nm after the storage (SI, Figure S6). These observations demonstrate that the resulting water-dispersible QDs-NH_2 have superior colloidal stability for long-term storage. Overall, the QDs-NH_2 show better properties than QDs-OMe (i.e., higher PLQYs, longer average exciton lifetime, smaller hydrodynamic sizes), which is likely due to a better passivation of surface metal dangling orbitals since QDs-NH_2 have a higher average ligand density than QDs-OMe, as discussed above (SI, Figure S5). For comparison, we also performed exchange of native ligands for other common hydrophilic surfactants (i.e., 11-mercaptoundecanoic acid and cysteine) (Supporting Information, Figure S7). The QDs-NH_2 shows the highest PLQY (44 ± 4%), while the QDs capped by small molecules show lower PLQYs (<10%). After 180 days of storage in the dark at 4 °C (QD concentrations, ~10 μM), the PLQYs of QDs-NH_2 were still nearly 80% of the initial value. In contrast, the 11-mercaptoundecanoic acid or cysteine-capped QD suspensions became turbid and exhibited PLQYs below 5% (Supporting Information, Figure S7).

QD−Dark Quencher FRET Pairs. The schematic diagram in Figure 5a shows the conjugation of amine-functionalized $CuInS_2$/ZnS QDs and IRDye QC-1 dark quencher molecules (Supporting Information, Figure S8) via NHS reaction chemistry. Herein, a side-by-side comparison experiment was performed by using amine-functionalized QDs-NH_2 and control methoxy-functionalized QDs-OMe for targeting the dark quencher dye molecules in a dye/QD feeding molar ratio from 0 to 20 (see the Experimental Section for details). After removal of the free dye molecules and byproducts by size-exclusion chromatography, the product QD−dye conjugate suspensions show obvious differences in color: green for QDs-NH_2−dye conjugates and nearly colorless for QDs-OMe−dye conjugates (Supporting Information, Figure S9). The corresponding absorption and PL spectra and PL decay curves of QD−dye conjugates were measured (Figure 5b−g). In the case of QDs-OMe, very small absorbances (<0.03) at ~740 nm (a characteristic peak of IRDye QC-1, Supporting Information, Figure S8) are observed upon increasing the dye/QD feeding molar ratio up to 20 (Figure 5b). These low absorbance values indicate negligible binding efficiencies, as expected for methoxy-functionalized dyes since the −OMe group is unable to react with the −NHS moieties in the IRDye QC-1 dye

DOI: 10.1021/acs.jpcc.9b10536
J. Phys. Chem. C 2020, 124, 1717−1731

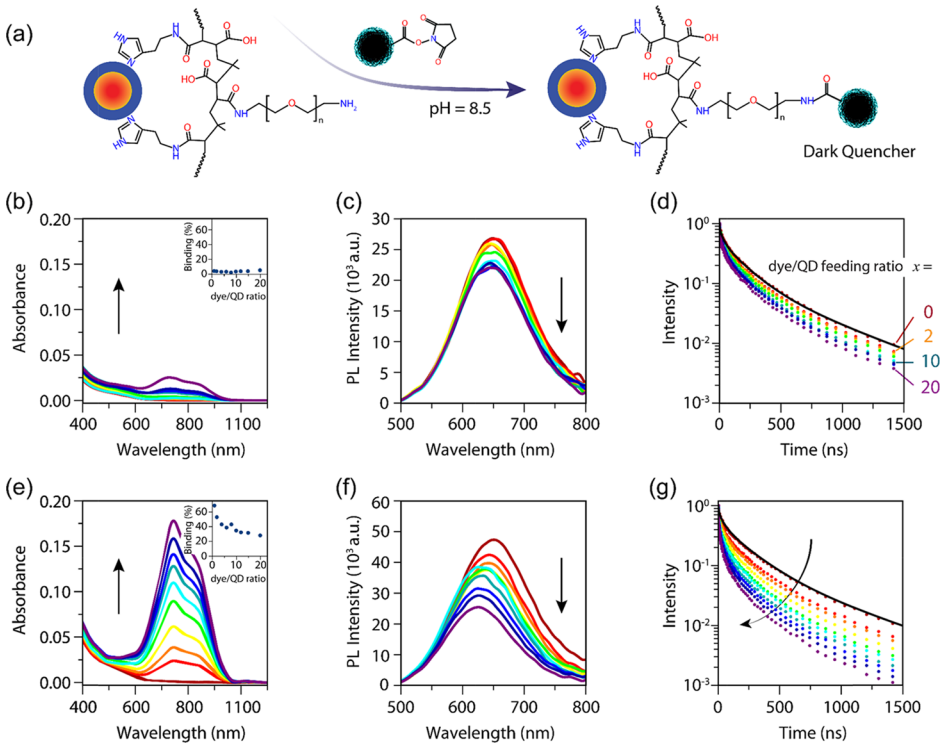

Figure 5. (a) Schematic diagram of the conjugation between QDs-NH_2 and the IRDye QC-1 dark quencher molecule through NHS ester reaction at pH = 8.5. (b–d) Absorption and PL spectra and PL decay curves of QDs-OMe–dye conjugates with an increase of the dye/QD feeding ratio from 0 to 20. Inset in (b) is the binding efficiencies of dye molecules to QDs-OMe (average value of 3.2%). They were calculated by comparing the experimental dye/QD ratio to the nominal dye/QD feeding ratio. Logarithmic binning was used for the PL decay curves to improve the signal-to-noise ratio at long times. A four-exponential decay function $[A_1e^{-t/\tau_1} + A_2e^{-t/\tau_2} + A_3e^{-t/\tau_3} + A_4e^{-t/\tau_4}]$ is used to describe the PL decay to the data without dye molecules (solid black lines), without giving any particular interpretation to the four exponents. (e–g) Same analysis as that in (b–d), but for QDs-NH_2–dye conjugates. The arrows in (b–g) indicate the trends upon increasing the dye/QD feeding ratio.

molecules. In contrast, the conjugates using QDs-NH_2 show a progressive increase of the absorption peak of the dark quencher dye, indicating that an increasing number of dye molecules are immobilized to the QDs (Figure 5e).

The average dye coverage densities on the QDs are estimated by absorption spectrophotometric analysis of the QD–dye conjugates using extinction coefficients of the QDs ($\sim 1.2 \times 10^5$ M^{-1} cm^{-1} at 400 nm[34]) and the dye molecules (9.6×10^4 M^{-1} cm^{-1} at 737 nm[47]), irrespective of the influence of FRET on their absorption/excitation characteristics. The extinction coefficients of the $CuInS_2$/ZnS QDs are estimated considering that the light absorption of the QDs at 400 nm is only related to the $CuInS_2$ cores, not to the ZnS shell. As discussed above, the effective diameter of the $CuInS_2$ cores (2.3 nm), deduced from the first absorption transition energies and the sizing curve reported in the literature,[34] was used for calculating the extinction coefficients of the $CuInS_2$/ZnS core/shell QDs, instead of the original diameter of the $CuInS_2$ cores (3.1 nm). The extinction coefficients of $CuInS_2$ QD cores at 400 nm can then be estimated following the size-dependent trends reported in the literature for wurtzite $CuInS_2$ QDS ($\varepsilon_{3.1eV} = 10175d^3$).[34] As discussed in ref 34, the size dependence of the extinction coefficients far above the band-edge is not significantly different for wurtzite and chalcopyrite $CuInS_2$ since the absorption cross section per formula unit of wurtzite $CuInS_2$ is close to that of chalcopyrite $CuInS_2$.[34]

The analysis of the average dye coverage density on the QDs is somewhat complicated by the fact that not only the QDs but also the dark quencher dye absorbs (weakly) at 400 nm. We account for this by subtracting the absorption contribution of the dark quencher from that of the mixture. Using this procedure, we estimate that the binding efficiencies of the dye molecules to QDs-OMe (i.e., the ratio between the number of bound dye molecules per QD and the nominal feeding molar ratio) are very low (3.2%) and essentially the same for all feeding ratios, indicating minimal nonspecific adsorption of the dye molecules onto QDs (inset in Figure 5b). In sharp contrast, the binding efficiencies of the dye molecules to QDs-NH_2 decrease upon increasing the dye/QD feeding molar ratio with a much higher average value of 41% (inset in Figure 5e). The clear differences in suspension color (Supporting Information, Figure S9) and binding efficiencies (Figure 5b,e) of the two sets of experiments demonstrate that the QDs-NH_2 is indeed linked to the dark quencher dye molecules through covalent bonds with the NHS group while the QDs-OMe shows no indication of binding, which is consistent with the functionality of the designed polymer ligands. The number of dye molecules per QD (e.g., ~5 dyes per QD for a nominal dye/QD feeding ratio of 20) is lower than the number of amine groups per QD estimated by NMR spectroscopy analysis (~39). Similar observations are rather common and reflect the fact that coupling reactions are not 100% efficient, typically requiring the use of excess reagents to increase the binding efficiency.[23] It is also possible that some amine groups coordinate directly onto the QD surface since the Zn^{2+}–NH_2 coordinating bond is quite strong.[64]

Intriguingly, the PL spectra are observed to blueshift upon increasing the dark quencher dye to QD ratio (Figure 5c and,

DOI: 10.1021/acs.jpcc.9b10536
J. Phys. Chem. C 2020, 124, 1717–1731

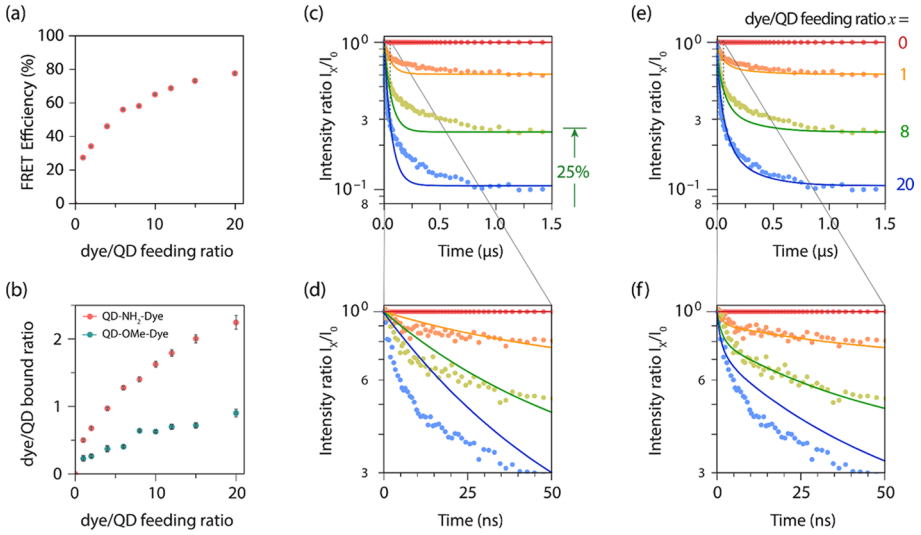

Figure 6. (a) Overall FRET efficiency of QDs-NH_2−dye conjugates upon increasing the amount of dark quencher dye molecules conjugated to QDs. The FRET efficiencies are estimated from the integrated intensity of the PL decay curves shown in Figure 5g using eq 1. The gray error bars are generated from the integration errors. (b) Average dye molecules per QD calculated from eqs 2 and 3 versus the feeding ratio of dye/QD in QD-OMe−dye (green dot) and QD-NH_2−dye (red dot) conjugates. The variations of the intensity ratio of I_x/I_0 (c−f) in the limit of sufficiently long times after the excitation pulse lead to larger uncertainties in estimation of the average dye molecules per QD. (c−f) Examples of PL decay curves of QD-NH_2−dye conjugates at different dye/QD feeding ratios x = 0 (red), 1 (yellow), 8 (green), and 20 (blue) divided by the reference curve at x = 0. (d, f) Zooms of (c) and (e), respectively. Four-exponential decay functions (solid lines) are used to describe the decays at different dye/QD feeding ratios, either considering the variations in nonradiative decay rates (model 1, (c, d)) or in radiative decay rates (model 2, (e, f)). The same analysis for QD-OMe−dye conjugates can be found in Supporting Information, Figure S12.

more clearly, Figure 5f). This is likely related to the polydispersity-induced heterogeneity of the QD emission wavelengths, which translates into different extents of overlap between the PL spectrum of the donor QD and the absorption spectrum of the acceptor dye (Supporting Information, Figure S8). For instance, larger QDs within the ensemble emit at lower energies, resulting in larger spectral overlaps with the dark quencher dye molecules, thereby leading to more efficient energy transfer and consequently more pronounced quenching of the QD PL, thus leading to bluing of the measured spectra due to removal of the contribution of the larger QDs. This quenching accompanied by spectral blueshifts also implies that energy transfer is the most plausible quenching mechanism rather than, for example, charge transfer. Moreover, reabsorption of the QD emission by the QD−dye conjugates is largely dependent on the emission wavelength, with lower energy emission being more strongly reabsorbed. For example, QDs-NH_2−dye conjugates (dye/QD = 20, Figure 5e) show 6.4 and 18.7% reabsorption at 645 and 745 nm over 0.5 cm (1 cm path length sealed quartz cuvettes were used), respectively. As a result, the emission spectra of the ensemble exhibit blueshifts, which are accompanied by slight narrowing of PL emission spectra (Supporting Information, Figure S10). Nevertheless, the PL bandwidths remain broad (~410 meV, Figure 5f and Supporting Information, Figure S10). This is consistent with broad single-particle emission linewidths that have recently been observed for individual $CuInS_2$-based QDs.[65] These broad single-particle linewidths can be understood considering that the emitting transition involves the recombination of a delocalized conduction band electron with a localized hole, being thus akin to a metal-to-ligand-charge-transfer transition, therefore coupling strongly to vibrations.[48,66]

The PL decay of the QDs becomes faster as the dye feeding ratio increases (Figure 5d,g). This confirms that the QD and dark quencher dye form donor−acceptor FRET pairs, in which the QD acts as the energy donor (D) and the dark quencher dye as the energy acceptor (A). The PL decay curves are clearly multiexponential, even in the absence of dark quencher dye (black curves in Figure 5d,g). This is a characteristic of $CuInS_2$-based QDs that has been reported in many previous studies, even for samples with PLQYs as high as 85%.[48,54,56,65−68] No consensus has yet been reached about the origin of the multiexponential character of the PL decay dynamics of $CuInS_2$-based QDs.[48] It may simply be related to variations in the nonradiative decay rate in different QDs in the ensemble, but it could also originate from intrinsic variations in the radiative decay rates of $CuInS_2$-based QDs due to variations in the location of the Cu-localized hole state involved in the QD emission.[48,67,68]

By analyzing the PL decay curves as a function of dye/QD feeding ratio, we can extract information about the dye binding and the FRET efficiencies. However, we have to take into account the intrinsic multiexponential nature of the excited-state dynamics of $CuInS_2$ QDs. For example, the expression

$$\eta = 1 - \frac{I_{D-A}}{I_D} = 1 - \frac{\tau_{D-A}}{\tau_D} \quad (1)$$

is often used to estimate the FRET efficiency η for a donor dye−acceptor dye FRET pair from the intensities (I) or lifetimes (τ) of donor emission, comparing the values in the absence (D) and in the presence (D−A) of acceptor molecules.[4,69] However, in contrast to dye molecules, $CuInS_2$ QDs show a wide variation in lifetimes even in the absence of FRET acceptors (black curves in Figure 5d,g). In addition, the QDs in the ensemble may bind a variable number of dark quencher dyes, resulting in a different FRET rate for each QD. In this case, the relation between average efficiency, average intensity, and average lifetime is not straightforward and does not exactly follow eq 1. Indeed, while eq 1 provides useful

DOI: 10.1021/acs.jpcc.9b10536
J. Phys. Chem. C 2020, 124, 1717−1731

rough estimates for the FRET efficiency, it yields higher values by a factor of 2−4 when using the donor lifetimes than when using the donor intensities extracted from the PL decay curves (Figure 6a and Figure S11). This illustrates that more in-depth analysis is necessary to understand the FRET process with $CuInS_2$ QD donors. It should be noted that the donor intensities extracted from the PL spectra in Figure 5 are less reliable because the dark quencher dye also weakly absorbs at the wavelengths used to excite the QDs (400−450 nm, see Supporting Information, Figure S8). We note that the rather weak quenching observed for the QD-OMe−dye system can be interpreted within the framework of solution-phase collisional quenching since the overall FRET efficiency increases linearly with the dye concentration, particularly in the low concentration regime (i.e., nominal dye/QD ratio ≤ 12, Supporting Information, Figure S11).[69]

Modeling of FRET Dynamics in $CuInS_2$-Based QD−Dye Conjugates. We introduce and apply two different models for the FRET dynamics with $CuInS_2$-based QD donors. For both, we first use a four-exponential decay function $[A_1e^{-t/\tau_1} + A_2e^{-t/\tau_2} + A_3e^{-t/\tau_3} + A_4e^{-t/\tau_4}]$ to describe the PL decay in the absence of a dark quencher dye (Figure 5d,g). We do not interpret the separate lifetime components here but realize that a fit function with any discrete number of lifetime components is a simple approximation to the (likely) continuous distribution that exists in the QD ensemble. Our aim here is to obtain a good analytical expression to the PL decay in the absence of FRET. We found that four exponentials provide an acceptable match to the experimental data. Thus, fitting the decay data using a higher number of exponentials is not necessary. Next, we assume that the conjugation of dye molecules to QDs follows Poisson statistics[19,70] due to variations in the number of binding sites per QD and in the occupation of the binding sites. The probability P that a QD has n dye molecules bound is then

$$P(n;\mu) = \frac{e^{-\mu}\mu^n}{n!}, \tag{2}$$

where μ is the average number dye molecules per QD. The value of μ is assumed to be independent of the lifetime of a QD; that is, dyes are equally likely to bind to fast-emitting and slow-emitting QDs. We chose the model of a Poisson distribution over a binomial distribution, which has previously also been used to model the distribution of bound molecules to QD surfaces.[71] Implementing a binomial model would force us to assume an upper limit to the number of bound dyes, which in reality likely does not exist because of a variation in the number of binding sites per QDs and the possibility of nonspecific binding.

We then use that, in the limit of sufficiently long times after the excitation pulse, all QDs have decayed, except those without dark quencher dyes attached. From the emission intensity at long times, we can thus extract the fraction of QDs with no acceptor molecules attached. More precisely,

$$\lim_{t\to\infty} \frac{I(t)}{I_0(t)} = P(0;\mu) = e^{-\mu} \tag{3}$$

where $I(t)$ is the normalized PL decay curve of the sample and $I_0(t)$ is the normalized reference measurement on the donor-only system (i.e., QDs without dye added). The use of the normalized PL decay curve of the donor-only system as reference makes it easier to quantify the changes induced by the interaction with the acceptor dyes regardless of the intrinsic multiexponential character of the PL decay of the donor QDs. Figure 6c−f shows $I(t)/I_0(t)$ for the QDs-NH_2 with various dye/QD feeding ratios (see Supporting Information, Figure S12 for the data for QDs-OMe). For illustration, $P(0;\mu) = 0.25$ is highlighted for the dye/QD feeding ratio of 8. From this analysis we can estimate μ and therefore the dye binding efficiency for each sample (Figure 6b). The values extracted in this way are ∼2 times smaller than those obtained from analyzing the absorption spectra (Figure 5e). This difference can be understood by considering that unconjugated dye molecules that were not completely removed by the washing procedure also contribute to the absorption spectra, while the PL decay curves are affected primarily by directly bound dye molecules. In this situation, the analysis of the PL decay curves provides a more accurate way to estimate the number of bound dye molecules per QD.

Next, we construct two possible models for the FRET dynamics from $CuInS_2$/ZnS QDs. The first starts from the assumption that the PL decay of $CuInS_2$-based QDs is multiexponential because of variations in nonradiative decay rates k_{nonrad} while the radiative decay rate k_{rad} is the same for all QDs in the ensemble. This is the conventional situation for dye molecules in which case the PLQY is the ensemble-average of $k_{rad}/(k_{rad} + k_{nonrad})$. In the second model, we assume that all PL decays we observe in the time-resolved PL profile are purely radiative and the multiexponential character arises from variations in radiative decay rates k_{rad}.[48,67,68] In this model, the PLQY is determined by a fraction of QDs in the ensemble that are entirely "dark"; that is, they absorb light but exhibit no emission.[72−75] These dark QDs do not contribute to the PL decay curve, but they do lower the PLQY of the ensemble. The presence of a fraction of dark QDs has been invoked to explain why shell growth on $CuInS_2$ QDs[76] or crown growth on CdSe nanoplatelets[77] strongly increases the PLQY, but does not affect the PL decay curve: shell or crown growth turns dark emitters bright but does not affect the decay dynamics of the bright ones. This also implies that for QDs, in contrast to typical dye molecules, the PLQY of the ensemble is not equal to the PLQY of the bright emitters that contribute to the PL decay curve. In fact, it has been shown in previous studies that the PLQY of bright QDs contributing to the PL decay curve is (nearly) unity even if the ensemble PLQY is lower.[78,79] The PL decay curve combined with the PLQY can therefore not be used to directly estimate the radiative and nonradiative decay rates of QDs.

Starting from these two possible models for the PL decay of our $CuInS_2$/ZnS QDs, we realize that FRET is based on dipole−dipole coupling, the rate of which scales linearly with the dipole strength and therefore the radiative decay rate of the donor.[80] If the nonradiative decay rate of the QDs varies while the radiative decay rate is constant (model 1), then the FRET rate k_{FRET} per QD−dye pair is the same for all QDs regardless of their PLQY. In contrast, if the radiative decay rate varies (model 2), then the FRET rate per QD−dye pair varies along with it. In the latter case, the Förster radius R_0 is the same for all QDs; in the former case, it is not.

Our model for the PL decay of $CuInS_2$-based QDs with varying nonradiative decay rates but constant FRET rate k_{FRET} per QD−dye pair (model 1) is

$$I(t) = \sum_i A_i \sum_n P(n;\mu) e^{-(k_i + nk_{FRET})t} \tag{4}$$

DOI: 10.1021/acs.jpcc.9b10536
J. Phys. Chem. C 2020, 124, 1717−1731

The summation i = 1, 2, 3, 4 runs over the different intrinsic QD decay rates (i.e., in the absence of dark quencher dye) in the sample and n = 0, 1, 2, ... over the possible number of dyes attached. A_i and k_i are fixed by the four-exponential fit to the reference data (Figure 5d,g).

Our model for the PL decay of $CuInS_2$-based QDs with varying radiative decay rates and the FRET rate varying along (model 2) is

$$I(t) = \sum_i A_i \sum_n P(n;\mu)\, e^{-k_i(1+nf)t} \tag{5}$$

where the factor f is the proportionality between the radiative decay rate k_i and the FRET rate fk_i. This correlation is only valid for FRET processes (i.e., energy transfer by dipole–dipole coupling) and is absent if the quenching is due to charge transfer between donor and acceptor.

Model 2 (variable radiative decay rate of the QDs; Figure 6e,f) fits the experimental data for the QDs-NH_2 samples better than model 1 (variable nonradiative decay rate of the QDs; Figure 6c,d). This implies that the observed quenching is indeed due to FRET between the donor QDs and the acceptor dyes and that the multiexponential character of the PL decay curves is due to variations in the intrinsic radiative lifetimes of the donor QDs. This latter aspect is consistent with the model recently proposed for the radiative recombination in $CuInS_2$ and other ternary I-III-VI_2 nanocrystals, which involves recombination of a delocalized conduction band electron with a hole localized at the group-I cation.[48,67,68]

The fit yields f = 3.2. Rewriting the FRET equation ($k_{FRET} = kR_0^6/R_{DA}^6$) where k is the donor radiative decay rate and R_{DA} the donor–acceptor distance, we obtain

$$R_{DA} = f^{-1/6} R_0 \tag{6}$$

The Förster radius of a donor–acceptor pair can be estimated using

$$R_0 = \left(\frac{9000(\ln 10)\kappa^2}{128\pi^5 N_A n_0^4} J \right)^{1/6} \tag{7}$$

where N_A is Avogadro's number, n_0 is the refractive index of the medium between donor and acceptor[81] (here, we estimate n_0 = 1.40 for PEG in water), the factor κ^2 = 2/3 accounts for dipole orientation averaging, and $J = 1.62 \times 10^{18}$ $M^{-1}cm^{-1}nm^4$ is the overlap integral between QD donor emission and dye acceptor absorption spectra (Supporting Information, Figure S13). This gives R_0 = 7.9 nm for the QDs–dye FRET pair. From this value and the fit result of Figure 6e,f, we estimate that the donor–acceptor distance in the QD-NH_2 system is R_{DA} = 6.5 nm. This matches well the distance estimated from the combination of the QD radius and the coating amine-functionalized polymer. Note that in eq 7, we did not include a correction for the finite ensemble PLQY of our QDs, which would appear if we applied the standard equation often used to estimate the Förster radius for donor–acceptor dye pairs.[69] We leave out this correction because our analysis of Figure 6 is consistent with the model of a dark and bright QD fraction in the ensemble (see discussion above). This implies that FRET in QD–dye conjugates will only take place between the bright QDs in the ensemble, with a PLQY of near unity,[78,79] and the acceptor dye molecules. We note that if the ensemble PLQY of 44% for the QD-NH_2–dye system is included in eq 7, slightly lower estimates of R_0 = 6.9 nm and R_{DA} = 5.7 nm would be obtained.

FRET efficiencies in multiacceptor systems were previously analyzed by our group using the expression

$$\eta = \frac{nf}{nf+1} \tag{8}$$

which depends on the FRET rate per acceptor, determined by $f = (R_0/R_{DA})^6$, and the number n of acceptors bound to a donor.[19] It is however important to realize that in the case of an inhomogeneous sample, eq 8 does not correctly describe the relationship between n, f and the average FRET efficiency η. This is clear from Figure 7 where we fit eq 8 (blue line) to the experimental FRET efficiencies. Adaptations to eq 8 are necessary to reproduce the dependence of FRET efficiency on the acceptor binding. We have shown above (Figure 6) that the FRET dynamics can be better reproduced assuming that the QDs vary in radiative decay rate but all have the same value of f. To correct eq 8 for the inhomogeneity in our sample would thus only require explicit averaging over the distribution of n, while f is kept constant and therefore does not complicate the averaging procedure. Assuming a Poisson distribution of number of acceptors bound,[19] the expression for the average FRET efficiency $\langle\eta\rangle$ becomes

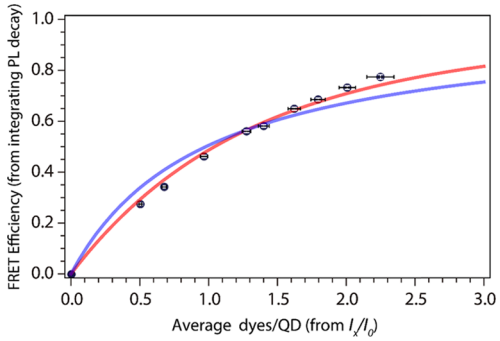

Figure 7. Overall FRET efficiency (obtained from integrating the total intensity contained in the PL decay curve) as a function of the average number μ of dye molecules per QD (obtained from eq 3). The data points (black) are fitted to eq 8 (blue line) and eq 9 (red line). The white and black error bars are the estimated errors of FRET efficiencies and average dye molecules per QD, respectively.

$$\langle\eta\rangle = \sum_n P(n;\mu)\, \frac{nf}{nf+1}, \tag{9}$$

where μ is the average number of bound dyes and $P(n;\mu)$ is given by eq 2. The model of eq 9 provides a good match (red line in Figure 7) to the experimental data. From this analysis of the FRET efficiency, we obtain f = 2.5, close to the value of f = 3.2 obtained from the analysis of the FRET dynamics. This corresponds to a difference of only 4% in the estimated donor–acceptor distance (R_{DA} = 6.8 nm versus R_{DA} = 6.5 nm). Considering the complex multiexponential PL decay dynamics of our system, this is an acceptable difference in estimated FRET parameters using two analysis methods. Our model, in which $CuInS_2$ QDs exhibit inhomogeneity in the radiative decay rates but constant Förster radius R_0, thus provides a consistent description of the properties of our FRET probes.

DOI: 10.1021/acs.jpcc.9b10536
J. Phys. Chem. C 2020, 124, 1717–1731

CONCLUSIONS

To conclude, we have reported here a multistep protocol that yields water-soluble FRET pairs using colloidal $CuInS_2$/ZnS QDs and IRDye QC-1 dark quencher dye molecules. NIR-emitting $CuInS_2$/ZnS QDs (PLQY of 55 ± 4%, peak at 645 nm) were synthesized through a combination of one-pot heating method and two ZnS shelling steps. These QDs were subsequently transferred into water by exchange of the native oleate ligands for two different types of polymer ligands (viz., methoxy-functionalized His-PIMA-PEG and amine-functionalized His-PIMA-PEG/NH_2). The product water-dispersible QDs-OMe and QDs-NH_2 have competitive PLQYs (27 ± 3%, peak at 660 nm and 44 ± 4%, peak at 650 nm, respectively), a compact hydrodynamic diameter of less than 20 nm, and excellent long-term colloidal stability (at least 10 months). These two types of polymer-capped QDs (QD-OMe and QD-NH_2) were subsequently conjugated to the IRDye QC-1 through NHS chemical reaction. The results confirm that QDs-NH_2 is conjugated with dark quencher dye molecules via covalent bonds, while the QDs-OMe binds only nonspecifically. The progressive quenching of the $CuInS_2$/ZnS QD emission and shortening of its exciton lifetime upon increasing the number of conjugated dye molecules demonstrate that the QD acts as the energy donor and the dark quencher dye as the energy acceptor in a donor-acceptor FRET pair. By assuming that the conjugation of dye molecules to QDs follows Poisson statistics, the average number of dye molecules per QD is estimated. Two different models based on the possible origin of the multiexponential character of the PL decay of $CuInS_2$-based QDs (i.e., variations in nonradiative or in radiative decay rates) were used to simulate the FRET dynamics of the QD−dye conjugates. The model based on variations in radiative decay rates provides a better fit of our experimental data. This suggests that the multiexponential character of the PL decay curves is due to variations in the intrinsic radiative lifetimes of the donor $CuInS_2$ QDs rather than to variations in the nonradiative decay rates. The model also estimates the donor−acceptor distance (6.5 nm), which matches well the hydrodynamic radius of the QDs-NH_2 prepared in our work. Overall, the quenching data collected for the present system can be interpreted within the framework of the Förster dipole−dipole coupling model, in line with previous reports on CdSe-based QD donors. This implies that $CuInS_2$-based QDs exhibit consistent mode of nonradiative transfer of excitation energy to proximal dyes by dipolar coupling despite their inherently broad emission spectra and long and multiexponential PL decays. This study sheds light on designing new efficient, Cd-free QD-based FRET nanoprobes, which are beneficial to a wide range of biological and biophysical studies such as biomedical imaging, photodynamic therapy, diagnostic and sensing devices.

ASSOCIATED CONTENT

Supporting Information

The Supporting Information is available free of charge at https://pubs.acs.org/doi/10.1021/acs.jpcc.9b10536.

^{1}H NMR spectra of multifunctional polymer ligands and polymer-capped $CuInS_2$/ZnS QDs; purity assessment of the product polymer ligands by NMR analysis; TEM images, band gap estimation, and FTIR spectra of $CuInS_2$ QDs before and after ZnS shell overgrowth; hydrodynamic size of QD-NH_2 after storing in the dark at 4 °C for 10 months; absorption and PL spectra of 11-mercaptoundecanoic acid and cysteine-capped $CuInS_2$/ZnS QDs; molecular structure and absorption spectrum of IRDye QC-1 dark quencher; digital images of the used G-25 columns and product QD−dye conjugate suspensions after the separation by size-exclusion chromatography; full width at half-maximum of PL emission spectra upon increasing the amount of dark quencher dye molecules attached to QDs; overall FRET efficiency of QDs-OMe−dye and QDs-NH_2−dye conjugates; plot of the spectral overlap and distance-dependent FRET efficiency in a QDs-NH_2−dye donor−acceptor pair; and FRET dynamic simulation for QDs-OMe−dye conjugates (PDF)

AUTHOR INFORMATION

Corresponding Author

*E-mail: c.demello-donega@uu.nl.

ORCID

Chenghui Xia: 0000-0001-5087-8805
Freddy T. Rabouw: 0000-0002-4775-0859
Hedi Mattoussi: 0000-0002-6511-9323
Celso de Mello Donega: 0000-0002-4403-3627

Present Addresses

$^{\parallel}$Laboratoire Photonique Numérique et Nanosciences, Univ. Bordeaux, UMR 5298, F-33400 Talence, France
$^{\perp}$Institut d'Optique & CNRS, LP2N UMR 5298, F-33400 Talence, France
§Xen Biofluidx Inc., 11494 Sorrento Valley Road, San Diego, California 92121, United States

Notes

The authors declare no competing financial interest.

ACKNOWLEDGMENTS

C.X. acknowledges China Scholarship Council (CSC) for financial support (No. 201406330055). C.d.M.D. acknowledges financial support from the division of Chemical Sciences (CW) of The Netherlands Organization for Scientific Research (NWO) under grant number ECHO.712.014.001. F.T.R. is supported by NWO Veni grant number 722.017.002 and by The Netherlands Center for Multiscale Catalytic Energy Conversion (MCEC), an NWO Gravitation program funded by the Ministry of Education, Culture and Science of the government of The Netherlands. The authors thank Johannes D. Meeldijk and Xiaobin Xie for high-resolution TEM measurements, Joep L. Peters for ^{1}H NMR measurements, and Gang Wang for XRD measurements.

REFERENCES

(1) Wegner, K. D.; Hildebrandt, N. Quantum Dots: Bright and Versatile *in vitro* and *in vivo* Fluorescence Imaging Biosensors. *Chem. Soc. Rev.* **2015**, *44*, 4792−4834.
(2) Skajaa, T.; Zhao, Y.; van den Heuvel, D. J.; Gerritsen, H. C.; Cormode, D. P.; Koole, R.; van Schooneveld, M. M.; Post, J. A.; Fisher, E. A.; Fayad, Z. A.; et al. Quantum Dot and Cy5.5 Labeled Nanoparticles to Investigate Lipoprotein Biointeractions *via* Förster Resonance Energy Transfer. *Nano Lett.* **2010**, *10*, 5131−5138.
(3) Medintz, I. L.; Uyeda, H. T.; Goldman, E. R.; Mattoussi, H. Quantum Dot Bioconjugates for Imaging, Labelling and Sensing. *Nat. Mater.* **2005**, *4*, 435−446.
(4) Hildebrandt, N.; Spillmann, C. M.; Algar, W. R.; Pons, T.; Stewart, M. H.; Oh, E.; Susumu, K.; Díaz, S. A.; Delehanty, J. B.;

DOI: 10.1021/acs.jpcc.9b10536
J. Phys. Chem. C 2020, 124, 1717−1731

Medintz, I. L. Energy Transfer with Semiconductor Quantum Dot Bioconjugates: A Versatile Platform for Biosensing, Energy Harvesting, and Other Developing Applications. *Chem. Rev.* **2017**, *117*, 536−711.
(5) Hsu, C.-Y.; Chen, C.-W.; Yu, H.-P.; Lin, Y.-F.; Lai, P.-S. Bioluminescence Resonance Energy Transfer Using Luciferase-Immobilized Quantum Dots for Self-Illuminated Photodynamic Therapy. *Biomaterials* **2013**, *34*, 1204−1212.
(6) Bakalova, R.; Ohba, H.; Zhelev, Z.; Ishikawa, M.; Baba, Y. Quantum Dots as Photosensitizers? *Nat. Biotechnol.* **2004**, *22*, 1360−1361.
(7) Lucky, S. S.; Soo, K. C.; Zhang, Y. Nanoparticles in Photodynamic Therapy. *Chem. Rev.* **2015**, *115*, 1990−2042.
(8) Freyria, F. S.; Cordero, J. M.; Caram, J. R.; Doria, S.; Dodin, A.; Chen, Y.; Willard, A. P.; Bawendi, M. G. Near-Infrared Quantum Dot Emission Enhanced by Stabilized Self-Assembled J-Aggregate Antennas. *Nano Lett.* **2017**, *17*, 7665−7674.
(9) Petryayeva, E.; Algar, W. R. Multiplexed Homogeneous Assays of Proteolytic Activity Using a Smartphone and Quantum Dots. *Anal. Chem.* **2014**, *86*, 3195−3202.
(10) Long, F.; Gu, C.; Gu, A. Z.; Shi, H. Quantum Dot/Carrier−Protein/Haptens Conjugate as a Detection Nanobioprobe for FRET-Based Immunoassay of Small Analytes with All-Fiber Microfluidic Biosensing Platform. *Anal. Chem.* **2012**, *84*, 3646−3653.
(11) Crivat, G.; Da Silva, S. M.; Reyes, D. R.; Locascio, L. E.; Gaitan, M.; Rosenzweig, N.; Rosenzweig, Z. Quantum Dot FRET-Based Probes in Thin Films Grown in Microfluidic Channels. *J. Am. Chem. Soc.* **2010**, *132*, 1460−1461.
(12) Suzuki, M.; Husimi, Y.; Komatsu, H.; Suzuki, K.; Douglas, K. T. Quantum Dot FRET Biosensors that Respond to pH, to Proteolytic or Nucleolytic Cleavage, to DNA Synthesis, or to a Multiplexing Combination. *J. Am. Chem. Soc.* **2008**, *130*, 5720−5725.
(13) Sapsford, K. E.; Berti, L.; Medintz, I. L. Materials for Fluorescence Resonance Energy Transfer Analysis: Beyond Traditional Donor−Acceptor Combinations. *Angew. Chem., Int. Ed.* **2006**, *45*, 4562−4589.
(14) Geißler, D.; Linden, S.; Liermann, K.; Wegner, K. D.; Charbonnière, L. J.; Hildebrandt, N. Lanthanides and Quantum Dots as Förster Resonance Energy Transfer Agents for Diagnostics and Cellular Imaging. *Inorg. Chem.* **2014**, *53*, 1824−1838.
(15) Qiu, X.; Wegner, K. D.; Wu, Y.-T.; van Bergen en Henegouwen, P. M. P.; Jennings, T. L.; Hildebrandt, N. Nanobodies and Antibodies for Duplexed EGFR/HER2 Immunoassays Using Terbium-to-Quantum Dot FRET. *Chem. Mater.* **2016**, *28*, 8256−8267.
(16) Marin, R.; Labrador-Paéz, L.; Skripka, A.; Haro-González, P.; Benayas, A.; Canton, P.; Jaque, D.; Vetrone, F. Upconverting Nanoparticle to Quantum Dot Förster Resonance Energy Transfer: Increasing the Efficiency through Donor Design. *ACS Photonics* **2018**, *5*, 2261−2270.
(17) Bednarkiewicz, A.; Nyk, M.; Samoc, M.; Strek, W. Up-Conversion FRET from Er^{3+}/Yb^{3+}:$NaYF_4$ Nanophosphor to CdSe Quantum Dots. *J. Phys. Chem. C* **2010**, *114*, 17535−17541.
(18) Clapp, A. R.; Medintz, I. L.; Mauro, J. M.; Fisher, B. R.; Bawendi, M. G.; Mattoussi, H. Fluorescence Resonance Energy Transfer Between Quantum Dot Donors and Dye-Labeled Protein Acceptors. *J. Am. Chem. Soc.* **2004**, *126*, 301−310.
(19) Pons, T.; Medintz, I. L.; Wang, X.; English, D. S.; Mattoussi, H. Solution-Phase Single Quantum Dot Fluorescence Resonance Energy Transfer. *J. Am. Chem. Soc.* **2006**, *128*, 15324−15331.
(20) Shi, L.; De Paoli, V.; Rosenzweig, N.; Rosenzweig, Z. Synthesis and Application of Quantum Dots FRET-Based Protease Sensors. *J. Am. Chem. Soc.* **2006**, *128*, 10378−10379.
(21) Algar, W. R.; Malonoski, A.; Deschamps, J. R.; Blanco-Canosa, J. B.; Susumu, K.; Stewart, M. H.; Johnson, B. J.; Dawson, P. E.; Medintz, I. L. Proteolytic Activity at Quantum Dot-Conjugates: Kinetic Analysis Reveals Enhanced Enzyme Activity and Localized Interfacial "Hopping". *Nano Lett.* **2012**, *12*, 3793−3802.
(22) Kaiser, U.; Jimenez de Aberasturi, D.; Vázquez-González, M.; Carrillo-Carrion, C.; Niebling, T.; Parak, W. J.; Heimbrodt, W. Determining the Exact Number of Dye Molecules Attached to Colloidal CdSe/ZnS Quantum Dots in Förster Resonant Energy Transfer Assemblies. *J. Appl. Phys.* **2015**, *117*, No. 024701.
(23) Wang, W.; Kapur, A.; Ji, X.; Safi, M.; Palui, G.; Palomo, V.; Dawson, P. E.; Mattoussi, H. Photoligation of an Amphiphilic Polymer with Mixed Coordination Provides Compact and Reactive Quantum Dots. *J. Am. Chem. Soc.* **2015**, *137*, 5438−5451.
(24) Wang, W.; Ji, X.; Kapur, A.; Zhang, C.; Mattoussi, H. A Multifunctional Polymer Combining the Imidazole and Zwitterion Motifs as a Biocompatible Compact Coating for Quantum Dots. *J. Am. Chem. Soc.* **2015**, *137*, 14158−14172.
(25) Clapp, A. R.; Medintz, I. L.; Fisher, B. R.; Anderson, G. P.; Mattoussi, H. Can Luminescent Quantum Dots Be Efficient Energy Acceptors with Organic Dye Donors? *J. Am. Chem. Soc.* **2005**, *127*, 1242−1250.
(26) Yao, H.; Zhang, Y.; Xiao, F.; Xia, Z.; Rao, J. Quantum Dot/Bioluminescence Resonance Energy Transfer Based Highly Sensitive Detection of Proteases. *Angew. Chem., Int. Ed.* **2007**, *46*, 4346−4349.
(27) So, M.-K.; Xu, C.; Loening, A. M.; Gambhir, S. S.; Rao, J. Self-Illuminating Quantum Dot Conjugates for *in vivo* Imaging. *Nat. Biotechnol.* **2006**, *24*, 339−343.
(28) Medintz, I. L.; Mattoussi, H. Quantum Dot-Based Resonance Energy Transfer and Its Growing Application in Biology. *Phys. Chem. Chem. Phys.* **2009**, *11*, 17−45.
(29) Speranskaya, E. S.; Sevrin, C.; De Saeger, S.; Hens, Z.; Goryacheva, I. Y.; Grandfils, C. Synthesis of Hydrophilic $CuInS_2$/ZnS Quantum Dots with Different Polymeric Shells and Study of Their Cytotoxicity and Hemocompatibility. *ACS Appl. Mater. Interfaces* **2016**, *8*, 7613−7622.
(30) Pons, T.; Pic, E.; Lequeux, N.; Cassette, E.; Bezdetnaya, L.; Guillemin, F.; Marchal, F.; Dubertret, B. Cadmium-Free $CuInS_2$/ZnS Quantum Dots for Sentinel Lymph Node Imaging with Reduced Toxicity. *ACS Nano* **2010**, *4*, 2531−2538.
(31) Li, L.; Daou, T. J.; Texier, I.; Kim Chi, T. T.; Liem, N. Q.; Reiss, P. Highly Luminescent $CuInS_2$/ZnS Core/Shell Nanocrystals: Cadmium-Free Quantum Dots for *in vivo* Imaging. *Chem. Mater.* **2009**, *21*, 2422−2429.
(32) De Trizio, L.; Prato, M.; Genovese, A.; Casu, A.; Povia, M.; Simonutti, R.; Alcocer, M. J. P.; D'Andrea, C.; Tassone, F.; Manna, L. Strongly Fluorescent Quaternary Cu−In−Zn−S Nanocrystals Prepared from $Cu_{1-x}InS_2$ Nanocrystals by Partial Cation Exchange. *Chem. Mater.* **2012**, *24*, 2400−2406.
(33) Xia, C.; Meeldijk, J. D.; Gerritsen, H. C.; de Mello Donega, C. Highly Luminescent Water-Dispersible NIR-Emitting Wurtzite $CuInS_2$/ZnS Core/Shell Colloidal Quantum Dots. *Chem. Mater.* **2017**, *29*, 4940−4951.
(34) Xia, C.; Wu, W.; Yu, T.; Xie, X.; van Oversteeg, C.; Gerritsen, H. C.; de Mello Donega, C. Size-Dependent Band-Gap and Molar Absorption Coefficients of Colloidal $CuInS_2$ Quantum Dots. *ACS Nano* **2018**, *12*, 8350−8361.
(35) van der Stam, W.; Berends, A. C.; de Mello Donega, C. Prospects of Colloidal Copper Chalcogenide Nanocrystals. *ChemPhysChem* **2016**, *17*, 559−581.
(36) Zhang, F.; Lees, E.; Amin, F.; Rivera_Gil, P.; Yang, F.; Mulvaney, P.; Parak, W. J. Polymer-Coated Nanoparticles: A Universal Tool for Biolabelling Experiments. *Small* **2011**, *7*, 3113−3127.
(37) Bullen, C.; Mulvaney, P. The Effects of Chemisorption on the Luminescence of CdSe Quantum Dots. *Langmuir* **2006**, *22*, 3007−3013.
(38) Nagaraja, A. T.; Sooresh, A.; Meissner, K. E.; McShane, M. J. Processing and Characterization of Stable, pH-Sensitive Layer-by-Layer Modified Colloidal Quantum Dots. *ACS Nano* **2013**, *7*, 6194−6202.
(39) Liu, W.; Choi, H. S.; Zimmer, J. P.; Tanaka, E.; Frangioni, J. V.; Bawendi, M. Compact Cysteine-Coated CdSe(ZnCdS) Quantum

DOI: 10.1021/acs.jpcc.9b10536
J. Phys. Chem. C 2020, 124, 1717−1731

Dots for *in vivo* Applications. *J. Am. Chem. Soc.* **2007**, *129*, 14530−14531.
(40) Tamang, S.; Beaune, G.; Texier, I.; Reiss, P. Aqueous Phase Transfer of InP/ZnS Nanocrystals Conserving Fluorescence and High Colloidal Stability. *ACS Nano* **2011**, *5*, 9392−9402.
(41) Liu, W.; Greytak, A. B.; Lee, J.; Wong, C. R.; Park, J.; Marshall, L. F.; Jiang, W.; Curtin, P. N.; Ting, A. Y.; Nocera, D. G.; et al. Compact Biocompatible Quantum Dots *via* Raft-Mediated Synthesis of Imidazole-Based Random Copolymer Ligand. *J. Am. Chem. Soc.* **2010**, *132*, 472−483.
(42) Jańczewski, D.; Tomczak, N.; Han, M.-Y.; Vancso, G. J. Synthesis of Functionalized Amphiphilic Polymers for Coating Quantum Dots. *Nat. Protoc.* **2011**, *6*, 1546−1553.
(43) Medintz, I. L.; Clapp, A. R.; Mattoussi, H.; Goldman, E. R.; Fisher, B.; Mauro, J. M. Self-Assembled Nanoscale Biosensors Based on Quantum Dot FRET Donors. *Nat. Mater.* **2003**, *2*, 630−638.
(44) Conroy, E. M.; Li, J. J.; Kim, H.; Algar, W. R. Self-Quenching, Dimerization, and Homo-FRET in Hetero-FRET Assemblies with Quantum Dot Donors and Multiple Dye Acceptors. *J. Phys. Chem. C* **2016**, *120*, 17817−17828.
(45) Chen, C.; Corry, B.; Huang, L.; Hildebrandt, N. FRET-Modulated Multihybrid Nanoparticles for Brightness-Equalized Single-Wavelength Barcoding. *J. Am. Chem. Soc.* **2019**, *141*, 11123−11141.
(46) Algar, W. R.; Khachatrian, A.; Melinger, J. S.; Huston, A. L.; Stewart, M. H.; Susumu, K.; Blanco-Canosa, J. B.; Oh, E.; Dawson, P. E.; Medintz, I. L. Concurrent Modulation of Quantum Dot Photoluminescence Using a Combination of Charge Transfer and Förster Resonance Energy Transfer: Competitive Quenching and Multiplexed Biosensing Modality. *J. Am. Chem. Soc.* **2017**, *139*, 363−372.
(47) Peng, X.; Chen, H.; Draney, D. R.; Volcheck, W.; Schutz-Geschwender, A.; Olive, D. M. A Nonfluorescent, Broad-Range Quencher Dye for Förster Resonance Energy Transfer Assays. *Anal. Biochem.* **2009**, *388*, 220−228.
(48) Berends, A. C.; Mangnus, M. J. J.; Xia, C.; Rabouw, F. T.; de Mello Donega, C. Optoelectronic Properties of Ternary I−III−VI_2 Semiconductor Nanocrystals: Bright Prospects with Elusive Origins. *J. Phys. Chem. Lett.* **2019**, *10*, 1600−1616.
(49) Susumu, K.; Mei, B. C.; Mattoussi, H. Multifunctional Ligands Based on Dihydrolipoic Acid and Polyethylene Glycol to Promote Biocompatibility of Quantum Dots. *Nat. Protoc.* **2009**, *4*, 424−436.
(50) Mei, B. C.; Susumu, K.; Medintz, I. L.; Mattoussi, H. Polyethylene Glycol-Based Bidentate Ligands to Enhance Quantum Dot and Gold Nanoparticle Stability in Biological Media. *Nat. Protoc.* **2009**, *4*, 412−423.
(51) Li, L.; Pandey, A.; Werder, D. J.; Khanal, B. P.; Pietryga, J. M.; Klimov, V. I. Efficient Synthesis of Highly Luminescent Copper Indium Sulfide-Based Core/Shell Nanocrystals with Surprisingly Long-Lived Emission. *J. Am. Chem. Soc.* **2011**, *133*, 1176−1179.
(52) Park, J.; Kim, S.-W. $CuInS_2$/ZnS Core/Shell Quantum Dots by Cation Exchange and Their Blue-Shifted Photoluminescence. *J. Mater. Chem.* **2011**, *21*, 3745−3750.
(53) Nam, D.-E.; Song, W.-S.; Yang, H. Facile, Air-Insensitive Solvothermal Synthesis of Emission-Tunable $CuInS_2$/ZnS Quantum Dots with High Quantum Yields. *J. Mater. Chem.* **2011**, *21*, 18220−18226.
(54) Berends, A. C.; Rabouw, F. T.; Spoor, F. C. M.; Bladt, E.; Grozema, F. C.; Houtepen, A. J.; Siebbeles, L. D. A.; de Mello Donegá, C. Radiative and Nonradiative Recombination in $CuInS_2$ Nanocrystals and $CuInS_2$-Based Core/Shell Nanocrystals. *J. Phys. Chem. Lett.* **2016**, *7*, 3503−3509.
(55) Berends, A. C.; van der Stam, W.; Hofmann, J. P.; Bladt, E.; Meeldijk, J. D.; Bals, S.; de Mello Donega, C. Interplay between Surface Chemistry, Precursor Reactivity, and Temperature Determines Outcome of ZnS Shelling Reactions on $CuInS_2$ Nanocrystals. *Chem. Mater.* **2018**, *30*, 2400−2413.
(56) Xia, C.; Winckelmans, N.; Prins, P. T.; Bals, S.; Gerritsen, H. C.; de Mello Donegá, C. Near-Infrared-Emitting $CuInS_2$/ZnS Dot-in-Rod Colloidal Heteronanorods by Seeded Growth. *J. Am. Chem. Soc.* **2018**, *140*, 5755−5763.
(57) Kuo, K.-T.; Chen, S.-Y.; Cheng, B.-M.; Lin, C.-C. Synthesis and Characterization of Highly Luminescent $CuInS_2$ and $CuInS_2$/ZnS (Core/Shell) Nanocrystals. *Thin Solid Films* **2008**, *517*, 1257−1261.
(58) Zhang, A.; Dong, C.; Li, L.; Yin, J.; Liu, H.; Huang, X.; Ren, J. Non-Blinking (Zn)CuInS/ZnS Quantum Dots Prepared by *in situ* Interfacial Alloying Approach. *Sci. Rep.* **2015**, *5*, 15227.
(59) Andersson, M.; Hedin, J.; Johansson, P.; Nordström, J.; Nydén, M. Coordination of Imidazoles by Cu(II) and Zn(II) as Studied by NMR Relaxometry, EPR, far-FTIR Vibrational Spectroscopy and Ab Initio Calculations: Effect of Methyl Substitution. *J. Phys. Chem. A* **2010**, *114*, 13146−13153.
(60) Sundberg, R. J.; Martin, R. B. Interactions of Histidine and Other Imidazole Derivatives with Transition Metal Ions in Chemical and Biological Systems. *Chem. Rev.* **1974**, *74*, 471−517.
(61) Dubois, F.; Mahler, B.; Dubertret, B.; Doris, E.; Mioskowski, C. A Versatile Strategy for Quantum Dot Ligand Exchange. *J. Am. Chem. Soc.* **2007**, *129*, 482−483.
(62) Zhao, C.; Bai, Z.; Liu, X.; Zhang, Y.; Zou, B.; Zhong, H. Small GSH-Capped $CuInS_2$ Quantum Dots: MPA-Assisted Aqueous Phase Transfer and Bioimaging Applications. *ACS Appl. Mater. Interfaces* **2015**, *7*, 17623−17629.
(63) Rurack, K.; Spieles, M. Fluorescence Quantum Yields of a Series of Red and Near-Infrared Dyes Emitting at 600−1000 nm. *Anal. Chem.* **2011**, *83*, 1232−1242.
(64) Cooper, J. K.; Franco, A. M.; Gul, S.; Corrado, C.; Zhang, J. Z. Characterization of Primary Amine Capped CdSe, ZnSe, and ZnS Quantum Dots by FT-IR: Determination of Surface Bonding Interaction and Identification of Selective Desorption. *Langmuir* **2011**, *27*, 8486−8493.
(65) Whitham, P. J.; Marchioro, A.; Knowles, K. E.; Kilburn, T. B.; Reid, P. J.; Gamelin, D. R. Single-Particle Photoluminescence Spectra, Blinking, and Delayed Luminescence of Colloidal $CuInS_2$ Nanocrystals. *J. Phys. Chem. C* **2016**, *120*, 17136−17142.
(66) Knowles, K. E.; Hartstein, K. H.; Kilburn, T. B.; Marchioro, A.; Nelson, H. D.; Whitham, P. J.; Gamelin, D. R. Luminescent Colloidal Semiconductor Nanocrystals Containing Copper: Synthesis, Photophysics, and Applications. *Chem. Rev.* **2016**, *116*, 10820−10851.
(67) Zang, H.; Li, H.; Makarov, N. S.; Velizhanin, K. A.; Wu, K.; Park, Y.-S.; Klimov, V. I. Thick-Shell $CuInS_2$/ZnS Quantum Dots with Suppressed "Blinking" and Narrow Single-Particle Emission Line Widths. *Nano Lett.* **2017**, *17*, 1787−1795.
(68) Knowles, K. E.; Nelson, H. D.; Kilburn, T. B.; Gamelin, D. R. Singlet−Triplet Splittings in the Luminescent Excited States of Colloidal Cu^+:CdSe, Cu^+:InP, and $CuInS_2$ Nanocrystals: Charge-Transfer Configurations and Self-Trapped Excitons. *J. Am. Chem. Soc.* **2015**, *137*, 13138−13147.
(69) Lakowicz, J. R. *Principles of Fluorescence Spectroscopy*; 3rd Ed.; Springer Science & Business Media: New York, 2006.
(70) Tachiya, M. Application of a Generating Function to Reaction Kinetics in Micelles. Kinetics of Quenching of Luminescent Probes in Micelles. *Chem. Phys. Lett.* **1975**, *33*, 289−292.
(71) Morris-Cohen, A. J.; Vasilenko, V.; Amin, V. A.; Reuter, M. G.; Weiss, E. A. Model for Adsorption of Ligands to Colloidal Quantum Dots with Concentration-Dependent Surface Structure. *ACS Nano* **2012**, *6*, 557−565.
(72) de Mello Donegá, C.; Koole, R. Size Dependence of the Spontaneous Emission Rate and Absorption Cross Section of CdSe and CdTe Quantum Dots. *J. Phys. Chem. C* **2009**, *113*, 6511−6520.
(73) Fisher, B. R.; Eisler, H.-J.; Stott, N. E.; Bawendi, M. G. Emission Intensity Dependence and Single-Exponential Behavior in Single Colloidal Quantum Dot Fluorescence Lifetimes. *J. Phys. Chem. B* **2004**, *108*, 143−148.
(74) de Mello Donegá, C.; Hickey, S. G.; Wuister, S. F.; Vanmaekelbergh, D.; Meijerink, A. Single-Step Synthesis to Control the Photoluminescence Quantum Yield and Size Dispersion of CdSe Nanocrystals. *J. Phys. Chem. B* **2003**, *107*, 489−496.

DOI: 10.1021/acs.jpcc.9b10536
J. Phys. Chem. C 2020, 124, 1717−1731

(75) Ebenstein, Y.; Mokari, T.; Banin, U. Fluorescence Quantum Yield of CdSe/ZnS Nanocrystals Investigated by Correlated Atomic-Force and Single-Particle Fluorescence Microscopy. *Appl. Phys. Lett.* **2002**, *80*, 4033−4035.
(76) Pinchetti, V.; Lorenzon, M.; McDaniel, H.; Lorenzi, R.; Meinardi, F.; Klimov, V. I.; Brovelli, S. Spectro-Electrochemical Probing of Intrinsic and Extrinsic Processes in Exciton Recombination in I−III−VI_2 Nanocrystals. *Nano Lett.* **2017**, *17*, 4508−4517.
(77) Rabouw, F. T.; van der Bok, J. C.; Spinicelli, P.; Mahler, B.; Nasilowski, M.; Pedetti, S.; Dubertret, B.; Vanmaekelbergh, D. Temporary Charge Carrier Separation Dominates the Photoluminescence Decay Dynamics of Colloidal CdSe Nanoplatelets. *Nano Lett.* **2016**, *16*, 2047−2053.
(78) Kwadrin, A.; Koenderink, A. F. Gray-Tone Lithography Implementation of Drexhage's Method for Calibrating Radiative and Nonradiative Decay Constants of Fluorophores. *J. Phys. Chem. C* **2012**, *116*, 16666−16673.
(79) Lunnemann, P.; Rabouw, F. T.; van Dijk-Moes, R. J. A.; Pietra, F.; Vanmaekelbergh, D.; Koenderink, A. F. Calibrating and Controlling the Quantum Efficiency Distribution of Inhomogeneously Broadened Quantum Rods by Using a Mirror Ball. *ACS Nano* **2013**, *7*, 5984−5992.
(80) Henderson, B.; Imbusch, G. F. *Optical Spectroscopy of Inorganic Solids*; Clarendon Press: Oxford, 1989.
(81) Rabouw, F. T.; den Hartog, S. A.; Senden, T.; Meijerink, A. Photonic Effects on the Förster Resonance Energy Transfer Efficiency. *Nat. Commun.* **2014**, *5*, 3610.

DOI: 10.1021/acs.jpcc.9b10536
J. Phys. Chem. C 2020, 124, 1717−1731